# DESIGN, CONSTRUCTION, AND ASSESSMENT OF A NEUTRON SHIELD FOR CDMS TEST FACILITIES

**A THESIS**
**SUBMITTED TO THE FACULTY OF THE GRADUATE SCHOOL**
**OF THE UNIVERSITY OF MINNESOTA**
**BY**

**Roxanne Radpour**

**IN PARTIAL FULFILLMENT OF THE REQUIREMENTS**
**FOR THE DEGREE OF**
**MASTER OF SCIENCE**

VUK MANDIĆ

**Aug, 2011**

**Acknowledgements**

As I was told (quite a few times), completing my Masters project would be one of the most difficult tasks I would accomplish during my experience as a graduate student. Granted, one does not learn if something comes easy to them, so I can comfortably say that a GREAT DEAL was learned on my behalf. However, this project would have been infinitely more difficult without the guidance and help of a few people. To these people I give you here my insufficiently-expressed thanks.

I was quite fortunate to have been accepted into a group that demands a certain competence in several research fields. To have this fortune extended by having three of the most patient teachers I have ever interacted with is quite astounding, and, yet, that is what I was dealt. Vuk Mandic, my advisor, Hassan Chagani, my post-doc, and Jianjie Zhang, my fellow CDMS graduate student, have all spent hours teaching me physics, fielding my questions, and guiding me through the seemingly-endless amount of obstacles I encountered in my project. You have shown me what it means to think like a physicist in the midst of research, and this I will continue to strive to accomplish. Your great patience and detailed explanations encouraged me to ask many questions (which I was never without). I never felt that I could not approach any of you with a question, and, for this, you have my greatest thanks.

Thank you Matt Fritts, Angie Reisetter, and Lauren Hsu from the CDMS collaboration for assisting me with questions related to work in this thesis. Also, thanks must be given to Sean Vig, Peter Ness, and the UMN Physics & Astronomy Machine Shop for their tremendous help in the construction of the neutron shield.

Along with the excellent editing skills of Vuk, I also had wonderful help from Dan Endean and Ryo Namba in editing my thesis. Thank you for reading and providing your extremely insightful comments, and for entertaining discussions with me about my work and the physics in general.

Lastly, thank you to my friends and family who persisted in your encouragement throughout the duration of this project. Thank you for not chastising me too heavily as I sunk away to the sub-basement of Tate to work (avoiding contact from the outside world for extended periods of time). It will probably only be a matter of time before I set myself on something else and do the same. Thus, I appreciate your continuous understanding and love.

Until the next step...

**Abstract**

The Cryogenic Dark Matter Search (CDMS) experiment is an effort to detect dark matter in the form of weakly interacting massive particles (WIMPs). CDMS utilizes cryogenic semiconductor detectors in order to accomplish this. At the University of Minnesota the testing and characterization of these detectors is one of the main responsibilities. To further improve characterization of the detectors, it is important to reduce the number of background events from reaching the detector as best as possible. This is especially significant in the case of neutrons since they produce nuclear recoils in the crystal similar to what is expected of a WIMP; these signals would be indistinguishable from each other in the data. Thus, the project was to build a neutron shield made of high-density polyethylene which would surround the dilution refrigerator where the detector was operated. Data was taken with the detector exposed to a Cf-252 (neutron) source with and without the shield in order to determine the shielding capability of the polyethylene. The data was analyzed and the results demonstrated a consistent shielding effect on events appearing as nuclear recoils, suggesting that the neutron shield is fulfilling its desired purpose.

# List of Figures

# Contents

# Chapter 1

# The Role of Dark Matter

## 1.1 A Cosmological Introduction to Dark Matter

Dark matter is a continuous anomaly in physics due to its significant presence and frustrating elusiveness. Its dominance in the universe surpasses that of ordinary matter by about 5 times, and its influence on the structure and formation of the universe is overwhelming. The importance of the dark matter and its consequences cannot be overstated; surprisingly, awareness of its existence was null until Fritz Zwicky's discovery ([17], [16]) in the 1930's that the average dispersion velocity for certain galaxies was much too large for their visible amount of matter. This is one of the biggest deceptions in nature. There exists a mass of such formidable size and influence on large scale structures and yet direct detection of this substance has not been made.

In order to understand the role of dark matter in the universe, it would be good to review what is understood about the formation and evolution of the universe. To do so, we begin with the Friedmann-Robertson-Walker (FRW) metric:

$$d\tau^2 = -dt^2 + a^2(t)\left(\frac{dr^2}{1-k\,r^2} + r^2 d\theta^2 + r^2 sin^2\theta d\phi^2\right), \tag{1.1}$$

where $k$ is the curvature of the universe. In terms of curvature, the geometry of the universe can be described as open, closed, or flat ($k = -1, 1$, or 0, respectively). This metric (1.1) satisfies the cosmological principle constraint: the universe must look the same everywhere and the spatial component of the metric should be maximally symmetric.

To describe the universe in terms of space and time, we can use the Einstein field equations (EFE) (1.2). These equations describe how space and time are affected by the presence of matter and energy [3].

$$R_{\alpha\beta} - \frac{1}{2} g_{\alpha\beta} R + \Lambda g_{\alpha\beta} = 8\pi G_N T_{\alpha\beta} \tag{1.2}$$

where $R_{\alpha\beta}$ is the Ricci tensor, $R$ is the Ricci scalar, $g_{\alpha\beta}$ is a metric tensor of choice, and $T_{\alpha\beta}$ is the stress-energy tensor that describes the flow of enery and momentum density in the universe [34]. The symbol $\Lambda$ is defined as the cosmological constant and its presence in the EFE represents a constant energy density throughout the history of the universe. It is also referred to as dark energy. Using the (FRW) metric as $g_{\alpha\beta}$ in equation 1.2, we obtain the Friedmann equations that relate the energy density and pressure with the rate of expansion and acceleration of the universe ([34], [18]):

$$\frac{3\dot{a}^2}{a^2} + \frac{3kc^2}{a^2} - \Lambda c^2 = 8\pi G_N \rho \tag{1.3}$$

$$\frac{-2\ddot{a}}{a} - \frac{\dot{a}^2}{a^2} - \frac{kc^2}{a^2} + \Lambda c^2 = \frac{8\pi G_N p}{c^2}, \tag{1.4}$$

where $\frac{\dot{a}}{a}$ defines the Hubble parameter, $H$, which describes the expansion rate of the universe in terms of its scale factor, $a(t)$. Conventionally, we choose the normalization of $a$ to be $a(0) \equiv a_0 = 1$. The pressure and energy density of the universe are represented by $p$ and $\rho$, respectively. By combining the two Friedmann equations appropriately, we obtain:

$$\dot{\rho} + 3\frac{\dot{a}}{a}(\rho + p) = 0 \tag{1.5}$$

Assuming an equation of state for the universe that relates the pressure and energy density ($p = w\rho$), equation 1.5 can be solved to find the density of the universe as a function of $a$. In the equation of state $w$ is a parameter that allows us to identify different components of the universe: for radiation $w = 1/3$, for matter $w = 0$, for dark energy $w =$ -1 and for curvature $w =$ -1/3. Any combination of these can be used to describe $\rho$.

Using the equation of state to substitute out the pressure and solving equation 1.5 for $\rho$, we obtain:

$$\rho(t) = \sum_w \rho_{0,w} a^{-3(1+w)} \tag{1.6}$$

where $\rho_{0,w}$ is the energy density of a specific component at current time. Thus, equation 1.6 can describe the energy density of the contents of the universe at a certain point in time. Aware of these parameters and definitions we can look back to the first Friedmann equation (1.3) and substitute and isolate $H$ within the equation:

$$H^2 = \frac{8\pi G_N}{3} \sum_w \rho_{0,\omega} a^{-3(1+w)} - \frac{kc^2}{a^2} \tag{1.7}$$

From here we can develop it further to represent the components of the universe. The first

term in equation 1.7 is comprehensive in that it incorporates all of the different components, $w$, including dark energy. For the time considered the "current" epoch, i.e. today, $H^2 = H_0^2$. Observations are consistent with a flat universe ($k = 0$), and so the right-hand side becomes just $\frac{8\pi G_N}{3} \sum_w \rho_{0,\omega}$ because $a(t = 0)$ is 1. This is used to define a critical energy density which will become a useful parameter in the progression of the Friedmann equation:

$$\rho_{crit} = \frac{3H^2}{8\pi G_N} \tag{1.8}$$

$H^2$ can be factored out from the right-hand side of equation 1.7 which allows us to identify distinct density terms.

$$H^2 = H^2\Big(\sum_w \frac{\rho_{0,w}}{\rho_{crit}} - \frac{kc^2}{a^2H^2}\Big) \tag{1.9}$$

$$\Omega_w \equiv \frac{\rho_w}{\rho_{crit}} \tag{1.10}$$

$$\Omega_k \equiv -\frac{kc^2}{a^2H^2} \tag{1.11}$$

The symbol $w$ in $\Omega_w$ represents matter($m$), radiation($r$), and/or dark energy ($\Lambda$). $\Omega_k$ is an analogy for curvature in terms of energy density components. At different times during the evolution of the universe there is varying dominance of these components. Observational evidence shows that $\Lambda$ is currently the dominating energy density. Because $\Omega_w$ is the ratio of densities, all of the components parameterizing the universe must sum to 1:

$$\Omega_r + \Omega_m + \Omega_\Lambda + \Omega_k = 1 \tag{1.12}$$

As a matter of convention and convenience, the contributions of energy density are considered individually from the curvature component. Establishing from the above equation that

$$\Omega_k = 1 - \sum_w \Omega_w \tag{1.13}$$

we can rewrite the Friedman equation using the $\Omega$ components (setting $a_0$ to 1):

$$H^2(t) = H_0^2\Big(\sum_w \Omega_{w,0} a^{-3(1+w)} + (1 - \sum_w \Omega_{w,0})a^{-2}\Big) \tag{1.14}$$

Now we can vary the $w$ parameter to see how the universe would behave if we had dominance from different components. For example, let's observe single-component dominance in a flat universe ($k$=0). Recall that the physical significance of $w$ is its role in the equation of state that relates the energy density and the pressure of the universe. For single-component dominance,

the Friedmann equation can simplify to:

$$H^2 = \left(\frac{\dot{a}}{a}\right)^2 \propto a^{-3(1+w)} \tag{1.15}$$

From here we can see how the scale factor of the universe behaves as a function of time for different $w$'s (radiation, matter, and dark energy, respectively):

$$w = 1/3 \rightarrow a \propto t^{\frac{1}{2}} \tag{1.16}$$

$$w = 0 \rightarrow a \propto t^{\frac{2}{3}} \tag{1.17}$$

$$w = -1 \rightarrow a \propto e^{Ht} \tag{1.18}$$

If we did consider curvature ($\Omega_k \neq 0$) and it dominates over all other components,

$$w = -1/3 \rightarrow a \propto t \tag{1.19}$$

We see, then, that as time goes on, the component that will increase the scale factor dominantly will be the cosmological constant, $\Lambda$. Looking back to the Friedman equations 1.3 and 1.4, $\Lambda$ dominance causes a positive acceleration in the exponential expansion of the universe because $\frac{\ddot{a}}{a} > 0$. However, it is understood that the universe is not composed of only one component. Through experiments and observations scientists work to determine the value of each component so as to better understand their contributions to the expansion of the universe and to determine what this rate actually is. Dark matter is a significant contributor to the matter density component previously mentioned. In the following sections, the evidence of the existence of dark matter and its nature will be discussed.

## 1.2 Evidence of Existence of Dark Matter

One of the first pieces of evidence that suggested there was more to the universe than met the eye was the study of dispersion velocities of the Coma cluster by Zwicky [36]. Using the virial theorem, he calculated the average dispersion velocity of the galaxies in the cluster based on the galaxies' visible sizes. He measured their actual velocities and compared them with the dispersion velocity. His results showed that the average velocity for galaxies based on luminous matter was about two orders of magnitude smaller than the measured velocities. Convinced that this posed a serious problem, one of his suggestions to remedy this was that there was probably a dark matter in abundance to cause these alarmingly large difference. Zwicky, however, was skeptical of this solution: "None of the proposed theories is satisfying. All of them have been developed on a most hypothetical basis" [36]. Today, we see more evidence for the existence of dark matter to suggest that Zwicky's proposed theory was actually correct. Other sources for

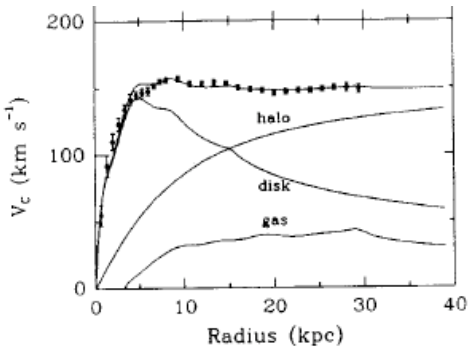


Figure 1.1: The figure above is an example of a galaxy rotation curve that has a constant velocity for an extensive distance beyond the visible galaxy radius. For this behavior to hold true a significant amount of invisible mass must be present [15].

suggestion come from rotation curves of spiral galaxies, which are measured from the spectral lines of neutral hydrogen in the galaxy. A sample of data on these rotation curves show the velocity reaching a constant value beyond the visible radius of the galaxies (Fig 1.1) [15].

This plateau corresponds to the mass of the galaxy increasing linearly with radius, as shown to a high degree in [25] , but this is not be possible unless there is an unaccounted for mass supporting these rotation curves. As further proof of missing matter, one can consider the evidence provided by elliptical galaxies. These galaxies contain x-ray emitting gases which provide insight into the temperature of the galaxy halo. Assuming thermal and hydrostatic equilibrium, the virial theorem can be applied to the stars to determine their velocities and compare this to the temperature of the x-ray emitting gases [18]:

$$v_s^2 = \frac{k_b T}{\mu m_p} \tag{1.20}$$

$\mu m_p$ is the average mass of the ions within the gas. If the relation above does not hold, then an inference can be made for missing matter. Measurements state that this relation in fact does not hold; rather, $T$ is proportional to $v_s^{1.45}$ [18]. These stars do not have the appropriate dispersion velocity to satisfy this behavior. Looking back to the virial theorem, this suggests that more mass must be necessary to satisfy this relationship.
Clearly, there is compelling evidence for missing matter. The cases above are just a few indications of the presence of dark matter. As to what this matter is made of is the next step in understanding its puzzling nature.

## 1.3 Nature of Dark Matter

As mentioned, dark matter particles have not yet been observed. The lack of experimental detection suggests that the interaction strength for these particles is on the order of the weak force. We also know that dark matter interacts through the gravitational force from observations of galaxy rotation curves. These unidentified particles we classify as WIMPs: Weakly Interacting Massive Particles.

Recall that the universe is comprised of different energy components: radiation, matter, and dark energy. The contribution of dark matter falls under $\Omega_m$. To know the amount of dark matter present, the total amount of matter in the universe should be determined. This can be measured by experiments such as WMAP (Wilkinson Microwave Anisotropy Probe) [2]. From there, distinctions between different types of matter must be made. Contributions to the matter density can be baryonic ($\Omega_b$) or non-baryonic ($\Omega_{nb}$). Baryonic matter is comprised of particles that are composed of 3 quarks, such as protons and neutrons. Typical non-baryonic particles are neutrinos and electrons. Dark matter seems to exist in abundance but, due to its lack of detection, its interaction and composition are unknown. However, some characteristic assumptions can be made from constraints determined from observations.

WIMPs can be categorized as relativistic or non-relativistic. We refer to these properties as hot or cold, respectively. Based on the structure formation of the universe, i.e. the development of galaxies, an argument can be made for the dominance of cold dark matter. If WIMPs are relativistic, the structures we see today would have been smeared out due to the streaming relativistic particles and we would have a much smoother universe. Keeping this in mind, we can next consider baryonic versus non-baryonic matter. The satellite WMAP has published data from an acquisition period of 7 years. This data places limits on different cosmological parameters; density parameters of different components in the observed universe are shown in Table 1.1 [2].

Table 1.1: Constraints on components of $\Omega_m$ [22] [2]

| **Component** | **Constraint)** |
|---|---|
| $\Omega_b$ | $0.0421 < \Omega_b < 0.0477$ |
| $\Omega_\Lambda$ | $0.705 < \Omega_\Lambda < 0.763$ |
| $\Omega_m$ | $0.237 < \Omega_m < 0.295$ |
| $\Omega_{lum}$ | $\leq 0.01$ |
| $\Omega_{DM}$ | $\geq 10^{*}\Omega_{lum} \geq 0.1$ |

Constraints on the amount of luminous and dark matter in the universe can be made by calculating the amount of visible mass within galaxies as well as their total mass inferred from their rotation. This provides energy density limitations for luminous matter ($\Omega_{lum}$), and for the

halo, which is assumed to consist predominantly of dark matter ($\Omega_{DM}$) (Table 1.1). As WMAP year 7 data gives the total mass density $\Omega = 1.001 \pm 0.058$ (with observational support that $k \sim 0$), some inferences can be made regarding the type of matter that dark matter consists of. By comparing the lower limit for $\Omega_{DM}$ and the upper limit for $\Omega_b$ there is a strong implication that dark matter is composed mostly of non-baryonic instead of baryonic matter. The leading candidates for cold non-baryonic WIMPs are neutralinos (suggested by supersymmetric models) and axions. As a side note, supersymmetric and extra-dimensions models predict very massive weakly interacting particles which makes WIMPs on the GeV scale a source of interest. Further discussions of these candidate particles can be found in [17] and [21].

# Chapter 2

# Detection

The various detection methods utilized in the search for the elusive WIMPs will be discussed in the following sections. Experiments such as DAMA and CDMS have a long history in this ongoing search and have seen several advancements in their detector technology. A WIMP must be detected directly or indirectly; in the non-relativistic limit, an elastic scattering with a nucleus would signify a direct detection while observing its signature through its annihilation products would be an indirect detection. When considering direct detection methods, one has to be aware that the scattering can be spin-dependent or spin-independent ([31], [17]). For spin-independent interactions the cross-section between the WIMP and the nucleon, $\sigma_{\chi N}$, will scale with the size of the nucleus ($\propto A^2$); to maximize this cross-section a target material with higher atomic numbers are preferred. However, for too large of nuclei the nuclear form factor, $F^2(q)$ (the Fourier transform of the nucleon density), used in the calculation of interaction rates, will suppress the interaction cross section [21]. To see this in a functional form, the differential detection rate [17], to be integrated over all possible incoming WIMP velocities and recoil energies of the nucleus, is

$$\frac{dR}{dE_r} = \int_v \frac{\sigma_{\chi N}\rho_\chi}{2\mu^2 m_\chi} F^2(q) \frac{f(v)}{v} dv \tag{2.1}$$

where $E_r$ is the recoil energy of the nucleus, $\rho_\chi$ is the density of WIMPs passing through the detector, $m_\chi$ is the mass of the WIMP, and $\mu$ is the reduced mass of the target nuclei and the WIMP.

Using equation 2.1, the range of recoil energy to be detected feasibly within experiments can be determined. Figure 2.1 shows the differential and total detection rate as a function of recoil energy for different detector types (Xe, Ge, S). Within the range of 80 keV it is clear that the detection rate drops at least an order of magnitude. To be able to detect a WIMP, then, experiments such as CDMS must restrict their searches to low energy ranges such as 10-100 keV.

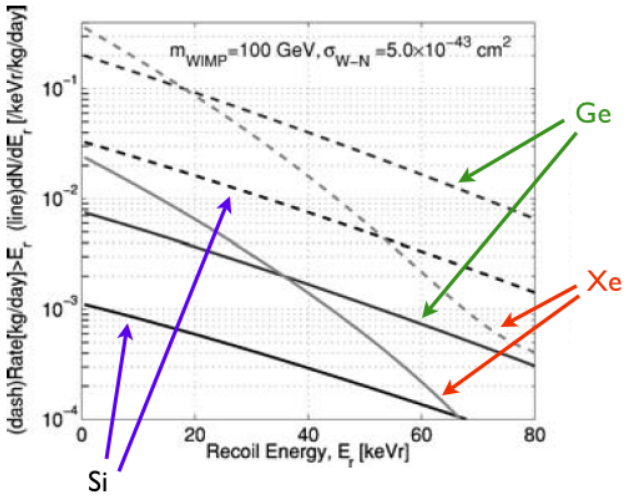


Figure 2.1: This plot shows the differential (solid line) and integrated (dashed line) rates for detecting a WIMP with a mass of 100 GeV and $\sigma = 5\text{x}10^{43}$ cm$^2$ for different target materials (Xe, Ge, Si $\rightarrow$ lightest to darkest lines). The recoil energy is plotted as a function of the nuclear recoil energy (in keV) of the target. For Ge, the detection rate drops almost an order of magnitude from 0-80 keV, which places a constraint on detection capabilities [17].

In direct detection dark matter experiments, the signal of a nuclear recoil in the target material is a possible indication of a WIMP interaction. However, this requires the ability to distinguish electron recoils from nuclear recoils. A few experiments and their detection methods will be discussed with the goal of understanding what the aim of their technique is in trying to detect WIMPs. To go about doing this, a specific detection method will be listed and an experiment utilizing this method will be discussed.

## 2.1 Solid Scintillators - DAMA

One type of detection technique involves the use of solid scintillators, and an ongoing experiment that has adopted this technique is the DAMA project. To infer the existence of WIMPs the experiment searched for a modulation signal that should repeat annually. This signal is observed due to the motion of the detectors through the dark matter halo. During the summer the Earth moves in the same direction as the Sun through the galaxy halo. The combined velocity of the Sun and Earth causes the Earth to have a larger velocity through the halo. In the winter the Earth's velocity is opposite of the Sun's which reduces Earth's overall velocity. The WIMP signal observed during the winter will therefore be smaller than the signal seen during the summer.

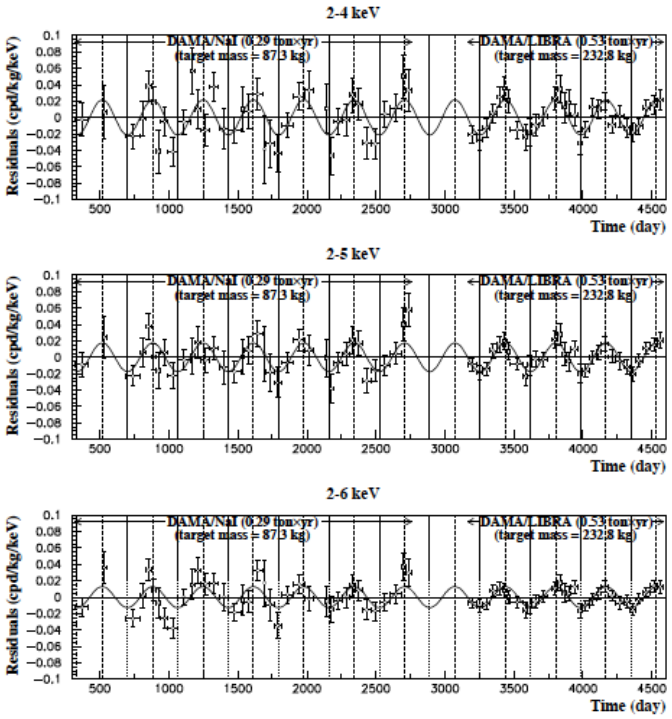


Figure 2.2: This figure shows the combined data of the former DAMA/NaI experiment and the new DAMA/LIBRA experiment. The data demonstrates a modulation signal which can be fitted with a cosine function of a period $T = 1$ year and a phase of 152.5 days [11]. A repetition of this experiment will take place in the South Pole to see if this signal can be observed again with a similar phase [9].

The most recent progression of DAMA, known as DAMA/LIBRA, uses twenty-five radiopure NaI(Tl) scintillator crystals as its target material. These scintillators are coupled with quartz light guides and photomultiplier tubes (PMTs) with a low energy trigger threshold [11]. Some of the advantages of the equipment and search method adopted by DAMA are the low backgrounds due to the high radiopurity crystals, the capability to scale the experiment to large masses, and the independence of the experiment's design from the theoretical models determining WIMP behavior and characteristics (though nuclear recoils are assumed for the detection in the crystals) [12]. A disadvantage, though, is that this technique observes a total event rate and is unable to distinguish between electron and nuclear recoils; thus, if a modulation signal is observed it might not necessarily be due to WIMPs. In 2008 DAMA announced their results, combining the data with their earlier experiment DAMA/NaI. According to Figure 2.2, a modulation pattern with a period of one year can be seen (more effectively in the DAMA/LIBRA segment). However, the WIMP-nucleon scattering cross section required to explain the DAMA signal is too large to be reconciled with the limits that experiments such as CDMS and XENON have placed. Because the signal observed by DAMA has not been observed by the other two experiments, a new experiment situated in the South Pole will search for the annual modulation signal to compare with DAMA's previous results [9].

## 2.2 Liquid Noble Detectors - XENON100

Liquid noble detectors have played a signficant role in the detection effort of dark matter due to their capability of trapping and detecting particles in the liquid effectively. When charges are produced in the noble liquid their magnitude is measured and these measurements provide 3-D image reconstruction of the particle interaction. Besides the imaging, other advantages of this technique are the low number of impurities due to the simple purification of the gaseous and liquid noble element, the variety of detection parameters that different noble liquids can provide, and the simple capability to scale the target mass higher [4]. XENON100 is one of the present experiments in the field of liquid noble detection. As implied by the name, this experiment utilizes 161 kg of liquid Xenon where 62 kg of this mass is the target material and the rest serves as the active veto for backgrounds entering the detector. When an interaction occurs in the target material, scintillation photons and ionization electrons are produced. Those photons are the first scintillation light detected; the ionized electrons drift through gaseous xenon situated above the liquid xenon and produce a second source of scintillation detected by PMTs above in the gas and at the bottom of the liquid. The 3-D imaging mentioned earlier is created by the location of the electron's detection on the PMTs and by the time it takes for it to move from the liquid xenon through to the PMTs in the gaseous xenon. The effectiveness of this double scintillation technique is that nuclear recoil events and electron recoil events have different amplitude ratios for the second light divided by the first light, which allows for

discrimination against dominant electromagnetic backgrounds that cause electron recoils [7]. With this developed technology, XENON100 has placed the most stringent upper limit on the spin-independent, elastic scattering cross section for the WIMP-nucleon interaction as 7.0 x $10^{-45}$ $cm^2$ for WIMP masses of 50 GeV/$c^2$.

## 2.3 Semiconductor Detectors - CDMS

Cryogenic semi-conductor detectors are detectors generally made of Si or Ge that detect nuclear recoils from scattering events at cryogenic temperatures ($<$ 50 mK) [14]. When there is an interaction in the bulk of the crystal two quantities are measured: charge ionization and phonon signals. Phonon sensors and charge electrodes arranged on the surfaces of the detector allow for the collection of these signals. A ratio of the ionization and recoil energy, defined as the ionization yield, allows for differentiation of electron and nuclear recoil events observed from different types of particle interactions. The Cryogenic Dark Matter Search (CDMS) has adopted this technology for their dark matter search and has made several progressions in the types of detectors used. For the latest results produced by CDMS II five towers with six ZIP (Z-dependent Ionization and Phonon) detectors were used. A newer and slightly different model of these detectors, known as iZIPs (i = interleaved), are currently under testing. The data discussed in this thesis was taken by a iZIP detector, G42. The structure and functions of the iZIP detectors will be described in the following sections.

#### Ionization Signal

On both faces of the detector there are two charge electrodes- an inner ($Q_i$) one that spans the bulk of the detector and an outer ($Q_o$) one in the form of a ring (Fig 2.3) [19]). When an event occurs within the crystal an electric field separates the electrons from the holes and causes them to drift to the charge electrodes. For ionization events occurring within the bulk of the crystal, the signal in $Q_i$ will be larger than $Q_o$. Ionization events that take place under the outer electrode have a larger $Q_o$ signal than $Q_i$. Because the electric field bias is not as uniform and the phonon sensor coverage is not as complete around the edge of the detectors, we reject $Q_o$ events which, in turn, allows us to define a fiducial detector volume [8].
Another part of the ionization signal to account for are the surface events. These events are electron recoils that produce a smaller ionization signal because they occur on only one side of the detector (unlike bulk events which generate larger signals in the electrodes on both sides). Due to the reduced ionization signal a smaller yield is produced for these surface events, which make them susceptible to misidentification amongst the nuclear recoils. This issue has resulted in a significant effort in the analysis process to discriminate as many surface events and establish a proper misidentification rate.

### Phonon Signal

When a particle interacts with an electron or nucleus in the crystal a phonon signal is generated within the lattice. This signal is picked up by photolithographically-defined sensors placed on both sides of the detector (Fig 2.3). These Transition-Edge Sensors (TESs), made of tungsten, are distributed into 8 phonon channels (4 on each side of the crystal) (Fig 2.4). Each channel has 458 QETs (quasiparticle-assisted electrothermal feedback TES), and each of these QETs has a 2.4 $\mu$m strip of tungsten with 8 superconducting aluminum films connected to it (Fig 2.5). A phonon that hits the aluminum fins will create quasiparticles that will diffuse through to the tungsten. These quasiparticles will undergo an electron-electron interaction with the conduction electrons in the tungsten [8]. When the electron-electron interaction occurs, the temperature of the tungsten sensor will increase, thus increasing its resistance, which lowers the monitored current flowing through them and indicates a signal occurence. Charges from the ionization signal also produce phonon signals as they drift through the bulk of the crystal which are known as Neganov-Trofimov-Luke phonons. To determine the recoil energy of the event, the energy from the charge-induced phonon signal, which takes into account the voltage bias applied to the detector, must be subtracted:

$$E_{recoil} = E_{phonon} - Q\,V \tag{2.2}$$

where Q is the total amount of charge detected.
The phonon signal can also provide information on the location of the interaction. All 8 channels will record some energy due to an interaction in the crystal. To determine the location of the interaction, start times of phonon signals on one side of the crystal can be compared. The quickest start-time points to the channel under which the interaction took place.

### Combining the two signals

Using the phonon and ionization signals, a preliminary distinction can be made between electron recoil and nuclear recoil events. By plotting the ionization yield, several events bands are formed (Fig 2.6, top). Ideally, there would be two bands where the top band consists of events due to electron recoils and a lower band due to nuclear recoils which produce a smaller ionization signal. However, some electron recoils that occur near the surface of the detector can be misidentified as nuclear recoil events because of their reduced ionization. Thus, there are three types of events to consider.

To reject these surface recoils, the phonon pulse timing parameter is used to identify the quicker phonon pulses which correspond to the electron recoils nearest to the surface of the detector (Fig 2.6, bottom). This allows a further improvement of the misidentification rate of electron recoils. Before the discrimination of surface events, CDMS II's rejection rate for the

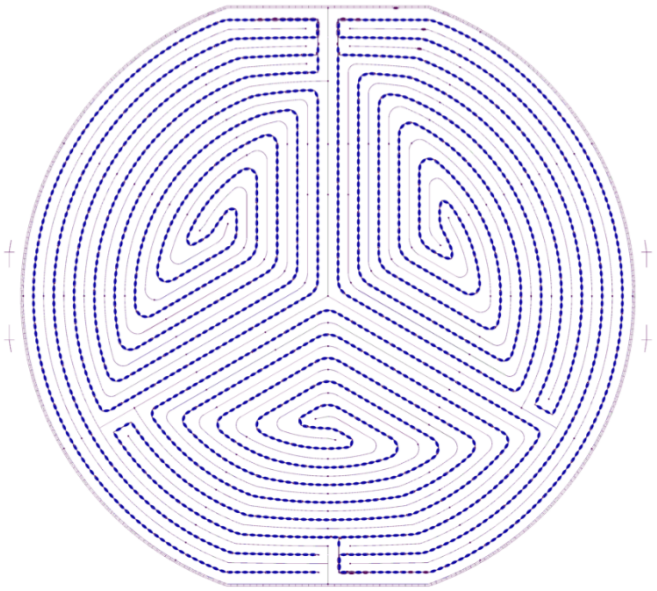

Figure 2.3: This is a 2-D view of one side of the iZIP detector. The phonon and charge channels are interwoven with one another (the charge channels are much fainter). $Q_o$ is the outer electrode that consists of a ring following the edge of the detector, and $Q_i$ spans the inner circular bulk of the detector.

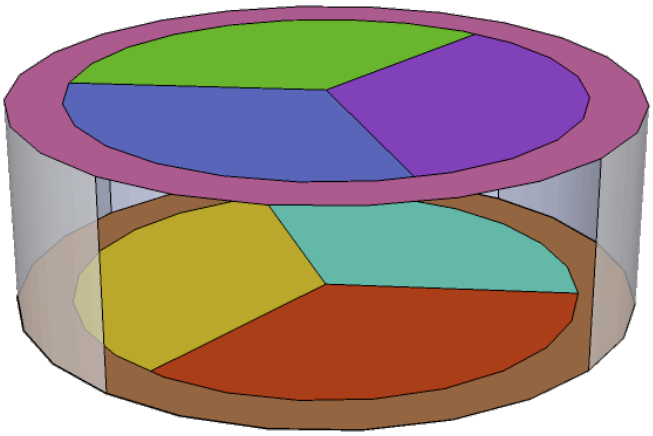

Figure 2.4: A 3-D view of the iZIP detector showing a simplified form of the 8 phonon channels. Channel A is the outer ring on each side of the detector, and channels B, C, and D consist of the 120° sections that cover the bulk of the detector. The 60° offset of the two sides' phonon channels provide non-degenerate position information of events [19].

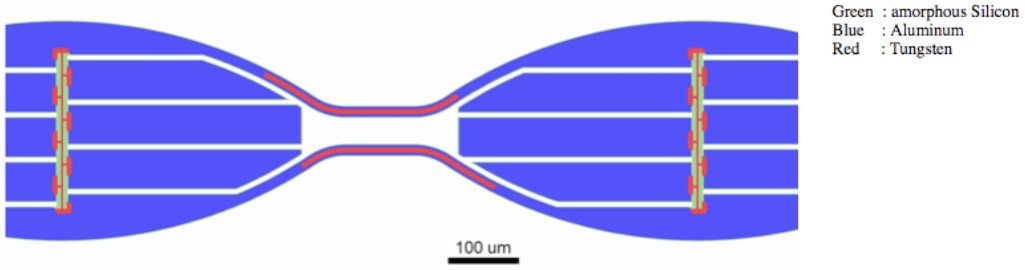


Figure 2.5: An example of a QET with a strip of tungsten and the 8 superconducting Al fins.

bulk electron recoils as determined by the ionization yield vs. the recoil energy is 1 in $10^4$. After applying cuts due to the ionization yield and timing parameter, the overall rejection rate for electron recoils was less than 1 in $10^6$ electron recoils.

CDMS's latest run was from July 2007 to September 2008 at the Soudan Underground Laboratory and this run utilized 19 Germanium and 11 Silicon ZIP detectors. Data from an exposure of 612 kg-days was used in the analysis. From this data there were two possible WIMP events observed[35]. The number of expected nuclear recoils due to the neutron background was $\sim 0.1$, and the number of electron recoils expected to be misidentified was $\sim 0.8$. Using Poisson statistics the likelihood of these two events being background events is 23%, which does not allow the collaboration to confidently say there has been an actual detection of dark matter. However, CDMS has also provided tight limits on the scattering cross-section to be $< 7.0$ x $10^{-44}$ cm$^2$ for a WIMP mass of 70 GeV/c$^2$ [13].

CDMS II and XENON100 have produced similar results that are in direct conflict with DAMA's results A comparison of different experiments' limits can be seen in Figure 2.7 .

## 2.4 Indirect Detection

The previous experiments adopted the direct detection approach. Experimental searches through indirect detection by observation of dark matter annihilation products have also been undertaken. These experiments search for signatures due to the self-annihilation of WIMPs which can appear in the form of anti-matter, neutrinos, and gamma rays [6].
Charged cosmic rays are made up of charged energetic particles that are produced from primary and secondary sources. Primary sources can be pulsars, microquasars, and dark matter annihilation [10]. Particles due to secondary interactions are produced from interactions between cosmic-rays nuclei and the inter-stellar medium. From the secondary sources there are rare products such as positrons, anti-protons, and anti-deuterons. Positrons, the least rare among

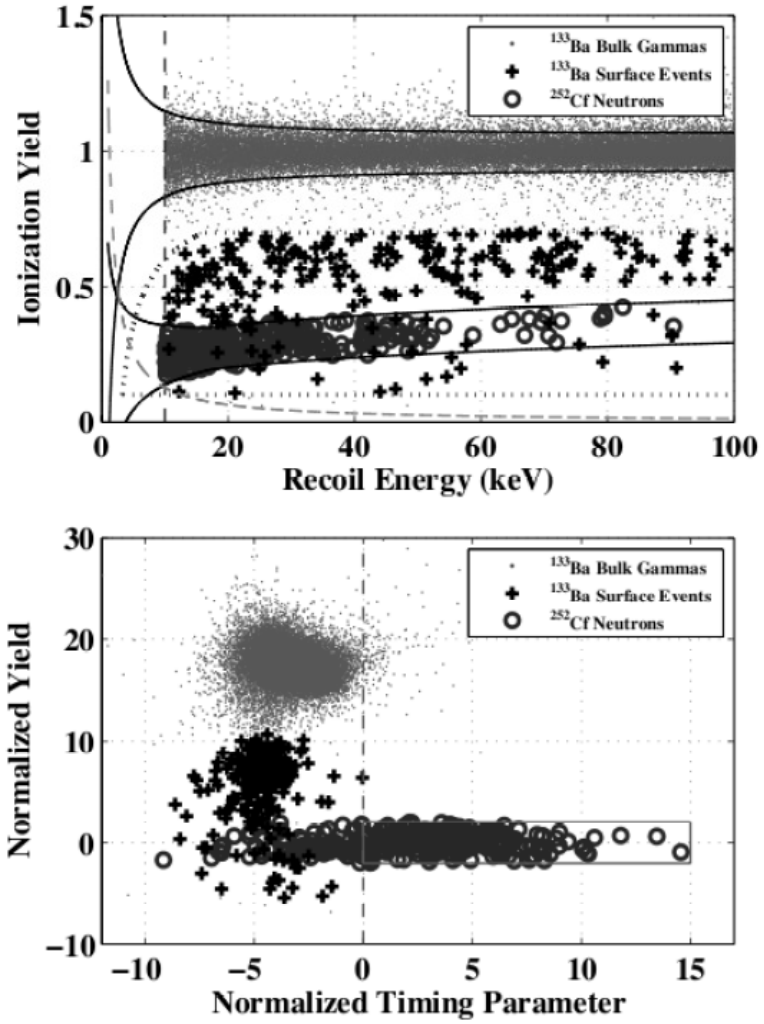


Figure 2.6: A plot of recoil events distributed according to their yield values from the latest CDMS results [35].

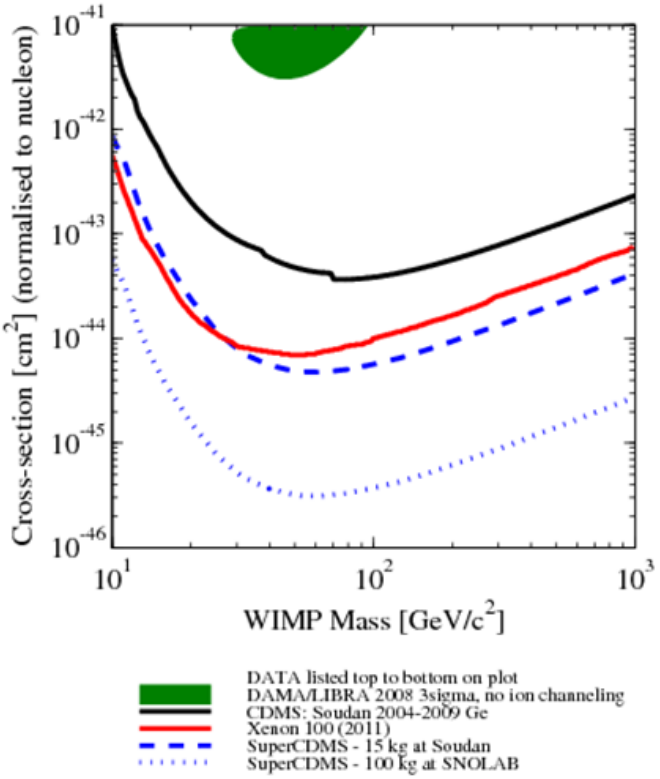


Figure 2.7: This plot [1] shows a comparison of the different limits on the WIMP-nucleon cross-section from the direct detection experiments discussed (CDMS II, DAMA/LIBRA, and XENON100). Thus far, XENON100 has placed the most stringent upper limit. There are also projections for the future science runs of CDMS (SuperCDMS).

the three, account for 0.1% of the total cosmic ray flux. Comparing background calculations of positrons due to cosmic rays to the measurements of the positron flux may reveal contributions of antimatter from unidentifiable sources. The satellite experiment PAMELA (Payload for Antimatter Matter Exploration and Light-Nuclei Astrophysics) has observed a noteworthy positron fraction, $\phi(e^+)/(\phi(e^+ + e^-)$, measurement in the range of 1.5-100 GeV (Fig. 2.8) [10]. A rapid increase in the fraction over most of the energy range contradicts behavior expected

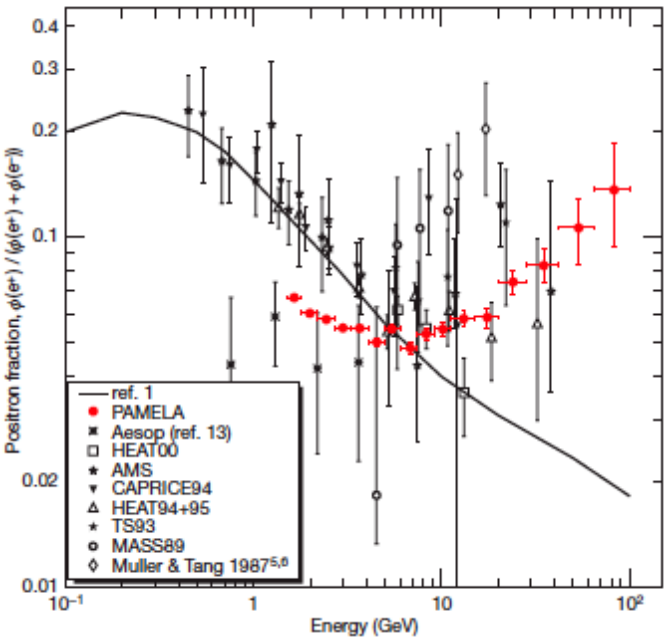


Figure 2.8: This figure demonstrates the sharp increase in the positron fraction observed by PAMELA. The solid curve represents the prediction model of the behavior of positrons due to secondary sources, which suggests that either PAMELA found events from a primary source or the model needs to be adjusted significantly.

from positrons observed due to secondary sources. This suggests that either models describing cosmic ray propagation need to be modified or that a primary source is producing these events. One of PAMELA's main efforts now is to be able to distinguish positrons produced from dark matter annihilation and astrophysical sources.

Gamma rays are beneficial to search for in dark matter experiments because they can point back to the location of their source. Their production comes from a bremsstrahlung process in the final state of WIMP annihilation into leptons. Electrons and positrons from annihilation also produce gamma rays through inverse Compton scattering. The Large Area Telescope (LAT) from the Fermi Gamma Ray Space Telescope searched for an excess of gamma rays in dense

galactic regions. Although not having found any significant evidence in terms of excess, upper limits have been placed on the gamma ray flux that could potentially be found [23].

Neutrino telescopes are also playing a part in the indirect detection effort by searching for neutrinos due to WIMP annihilation. In the annihilation process, the neutrinos can escape from the source regions of high density and, because of their weakly interacting nature, can provide insight to the location of the source. One such telescope is IceCube-DeepCore, located in the South Pole, which will search for these neutrino signals from the Earth, Sun, and the galactic center [28]. This Cherenkov detector spans a volume of 1 $km^3$ within the ice and consists of 86 strings that consist of 60 Digital Optical Modules (DOMs)[5]. IceCube, having also encompassed its predecessor experiment AMANDA, will have a heightened sensitivity towards solar WIMP signals and atmospheric neutrino oscillations [33]. However, the observation of solar WIMP presence is affected by the dominating atmospheric neutrino flux background and neutrinos due to cosmic rays; therefore, significant effort will be placed in understanding this background to distinguish it from potential annihilation events [5].

# Chapter 3

# Neutron Shield Development

## 3.1 Motivation

The project was based on the development of a neutron shield that would surround the dilution refrigerator in the UMN CDMS test facility. The motivation for this came from the necessity to understand and characterize the performance of CDMS detectors subject to various backgrounds. As discussed in Chapter 2, the detectors measure electron and nuclear recoils, and the phonon and ionization signals help to discriminate between the two types of recoils. Some of these electron recoils can be misidentified as nuclear recoils due to their reduced ionization signal, and a phonon timing parameter is used to reject these events as best as possible. This, in turn, allows a conclusion to be made on the probability of having completely distinguished the nuclear recoils from the electron recoils. To do this, it is necessary to know what the rejection efficiency is for a specific detector- each detector is unique in its ability to reject these deceiving electron recoils; thus, it is the goal of the test facilities to characterize the detector behavior as best as possible. At the UMN test facility a shield of polyethylene was to be built with the intention of conducting tests on the rejection of the surface electron recoil events with reduced ionization. If the detectors are always inundated with neutrons from cosmic rays and the environment, the ability to conduct a proper test on rejection efficiency will prove difficult since there will be a larger probability of nuclear recoils in the nuclear recoil band, affecting the efficiency measurement. If the shield can reduce the neutron flux by an order of magnitude, that would be a significant improvement for the characterization tests of the detector's rejection efficiency.

## 3.2 Material

Neutrons can interact through scattering or absorption, but, in terms of the present discussion the interaction by scattering is the relevant case. To reduce the incoming neutron flux to detectors the neutrons must collide with nuclei such that the particle's kinetic energy can be reduced significantly. As the neutrons penetrate further into the shield material, their kinetic energy will become progressively lower. To reduce the kinetic energy of the neutrons most effectively, it is best to have a proton-rich target since the proton and neutron effectively have the same mass, thus providing conditions for maximum energy transfer. The best choice for a proton-rich material should be hydrogenous in nature, and at our disposal was a large supply of high-density polyethylene sheets that were 1-inch in thickness and of varying height and width.

## 3.3 Shield Thickness Calculation

The general structure of the shield was determined- it was understood how the polyethylene would be placed around the shield and where the weaknesses in the shielding would lie. To finalize the structure, an effective thickness for the shield that would lower the neutron flux appropriately needed to be determined. To find an approximate thickness, an equation was developed to calculate the total number of neutrons passing through a shield of variable thickness. The neutron count can be calculated using their probability distribution function as a function of their energy (in this case, the recoil energy, $E_r$, of the detector target nuclei):

$$N_n = \int_{E_r} PDF(E_r) dE_r \tag{3.1}$$

This distribution function can be re-written in terms of the energy spectrum of the incoming neutrons, $S(E_n)$:

$$PDF(E_r) = S(E_n) \frac{dE_n}{dE_r} \frac{d\Omega}{4\pi} \tag{3.2}$$

As for $E_n$, the range of interest is determined from the recoil energy range of the Germanium nuclei within the detector, which is 10-100 keV (as discussed in Chapter 2). To find $E_n$ the collision between the neutron and the detector nuclei can be simplified to elastic scattering with averaging over the angle dependence. For this simplified case, the incoming energy for the neutrons can thus be represented as:

$$E_n = \frac{(m_n + m_r)^2 E_r}{2 m_r m_n} \tag{3.3}$$

where $m_r$ is the mass of the Germanium nuclei and $m_n$ is the mass of the neutron. At this point,

one could calculate the number of neutrons scattered off the detector without the impediment of the shield. As the neutron travels through the layers of polyethylene, its energy is going to be moderated exponentially. This, in turn, will reduce the flux of neutrons, $N$, detected. The exponential factor is a function of the polyethylene's attenuation factor, $\Sigma$, and the distance traveled by the neutron, $d$:

$$N = N_o\, e^{-\Sigma(E_n)d} \tag{3.4}$$

The attenuation factor is constructed as a linear combination of the energy-dependent cross-sections of hydrogen and carbon and is defined as:

$$\Sigma = (n_H\sigma_H + n_C\sigma_C) \times 10^{-24}\ \mathrm{cm}^{-1} \tag{3.5}$$

where the $\sigma_a$ is the cross-section for elastic scattering of an atom of type $a$, and $n_a$ is the number density of atom $a$ in the polyethylene. Keeping in mind that polyethylene is composed of $CH_2$ groups, the number density is defined as:

$$n_a = \frac{\rho_{poly}\, N_a\, b}{m_{CH_2}} \tag{3.6}$$

where $\rho_{poly}$ is 0.941 g/cm$^3$, $N_a$ is Avogadro's number, $m_{CH_2}$ is the molar mass of $CH_2$, and $b$ is the number of atoms of a specific type in $CH_2$. For hydrogen $b = 2$ and for carbon $b = 1$.
In order for the nuclei to recoil at a range of 10-100 keV, the incoming neutron energy should range from $\sim$ 0.4 - 4 MeV. These are fast neutrons; for low energy neutrons, the elastic cross-section can be considered constant [27]. As the energy of the neutron increases, the cross section will decrease, thus the need for the energy dependence of the cross-sections. The cross-sections for hydrogen and carbon were obtained for the ranges from 1-10 MeV from a study of neutron detectors by Mesquita et al. [24], who fitted a 6th order polynomial to data on hydrogen and carbon cross-sections:

$$\sigma_H = 6.94 - 4.48 * E_n + 1.6 * E_n^2 - 0.313 * E_n^3 + 0.0332 * E_n^4 - 0.00179 * E_n^5 + 0.0000385 * E_n^6 \tag{3.7}$$

$$\sigma_C = 9.70 - 13.5 * E_n + 8.22 * E_n^2 - 2.33 * E_n^3 + 0.330 * E_n^4 - 0.0228 * E_n^5 + 0.0061 * E_n^6 \tag{3.8}$$

Combining the above quantities appropriately (according to equation 3.6) the final form of the polyethylene attenuation factor in terms of $E_n$ (MeV) is:

$$\begin{aligned} \Sigma \;=\; & 0.938003 - 0.898396 * E_n + 0.458372 * E_n^2 - 0.118882 * E_n^3 \\ & + 0.0159624 * E_n^4 - 0.00106326 * E_n^5 + 0.000249851 * E_n^6\ \mathrm{cm}^{-1} \end{aligned} \tag{3.9}$$

Having identified the necessary parameters to calculate the neutron flux through a shield of

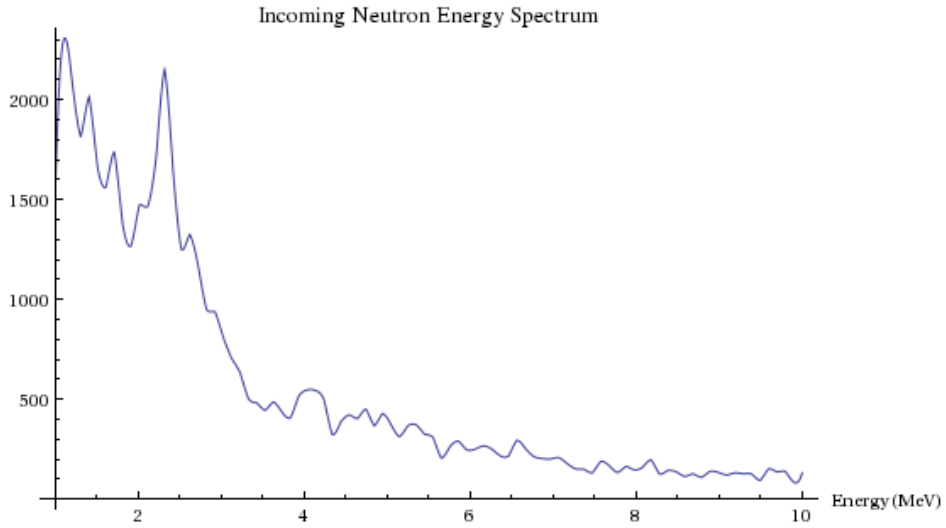


Figure 3.1: Energy spectrum for neutrons entering cavern at Soudan where CDMS experiment is held.

thickness $d$, the final generalized formula can be written as:

$$N_n = \int_{E_r} PDF'(E_r) dE_r = \int_{E_r} S(E_n) \frac{dE_n}{dE_r} \frac{d\Omega}{4\pi} e^{-\Sigma(E_r)d} dE_r \tag{3.10}$$

Note that $PDF'(E_r)$ is the new probability distribution function for the neutrons after the shield is introduced.

Determining the functional form of $S(E_n)$ is not trivial. The energy spectrum of the incoming neutrons is unknown for the UMN facility and so an approximation must be made by using known spectra from other sources. The absolute scaling of the spectrum, however, is not a concern since this factor will cancel in the final result of the shield analysis. A sample neutron flux can be used as a reference for these calculations in finding the theoretical shielding effect. An iZIP at the University of California, Berkeley (UCB) test facility detected a background count within the 10-100 keV range of 47 +/- 12 neutron events/ hour [29].

As for the neutron energy spectrum, two resources were considered. One spectrum models the neutrons with energies from 1-10 MeV entering the region where the CDMS experiment is held at Soudan Underground Laboratory (Fig. 3.1) [26]. This spectrum was developed from a Monte Carlo (MC) simulation of cosmogenic neutrons entering a region structured with CDMS geometry. It would be ideal to find an energy spectrum for neutrons at a depth closer to that of the UMN test facility. However, we can use the spectrum at Soudan as one option and conduct a comparison with another spectrum. A neutron energy spectrum at sea level would be an

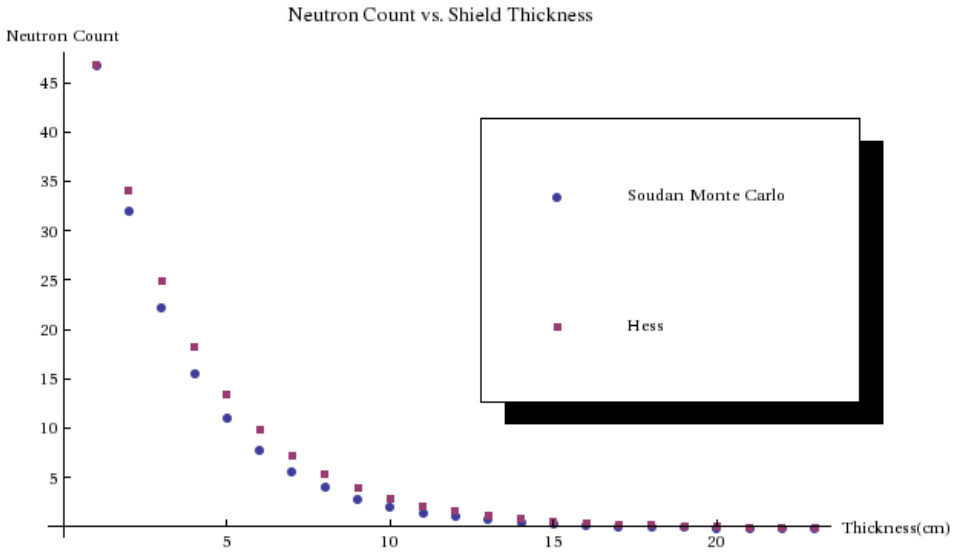


Figure 3.2: A comparison of calculations for the shield thickness necessary to reduce the flux of neutrons effectively. The red squares represent the results using the MC-generated energy spectrum (1-10 MeV). The blue dots represent the results using the energy spectrum from Hess' work (energies $> 1$ MeV).

appropriate test parameter in the comparison. Hess, et al, [20] carried out an experiment to find the energy spectrum of cosmic ray neutrons at various altitudes. They developed a production energy spectrum (in MeV) for neutrons with energies above 1 MeV that is a function of altitude. As an approximation, we can use the spectrum at sea level (atmospheric depth, $h$, $= 0$), which simplifies the spectrum to:

$$S(E_n, h) = \frac{C}{(50 + E_n)^2} \tag{3.11}$$

where $C$ is an overall constant and $E_n$ is in units of MeV.

Both of these spectrums are due to cosmogenic radiation, such as muons that decay into neutrons. Radioactive decay from the surrounding environment also occurs in which fission processes produce ambient neutrons. However, the contribution from cosmic rays are at least several orders of magnitude larger than neutrons from the radiogenic sources.

Figure 3.2 shows the reduction in neutron flux for the two spectra due to the neutron shield. These calculations both show that with approximately 10 cm of shield thickness the neutron flux for neutrons can be reduced by a factor of 10. We can compare these calculated values to a polyethylene manufacturer's, Shieldwerx, calculations of neutron moderation. Figure 3.3 [30] shows how to determine what thickness of polyethylene is needed in order to have the

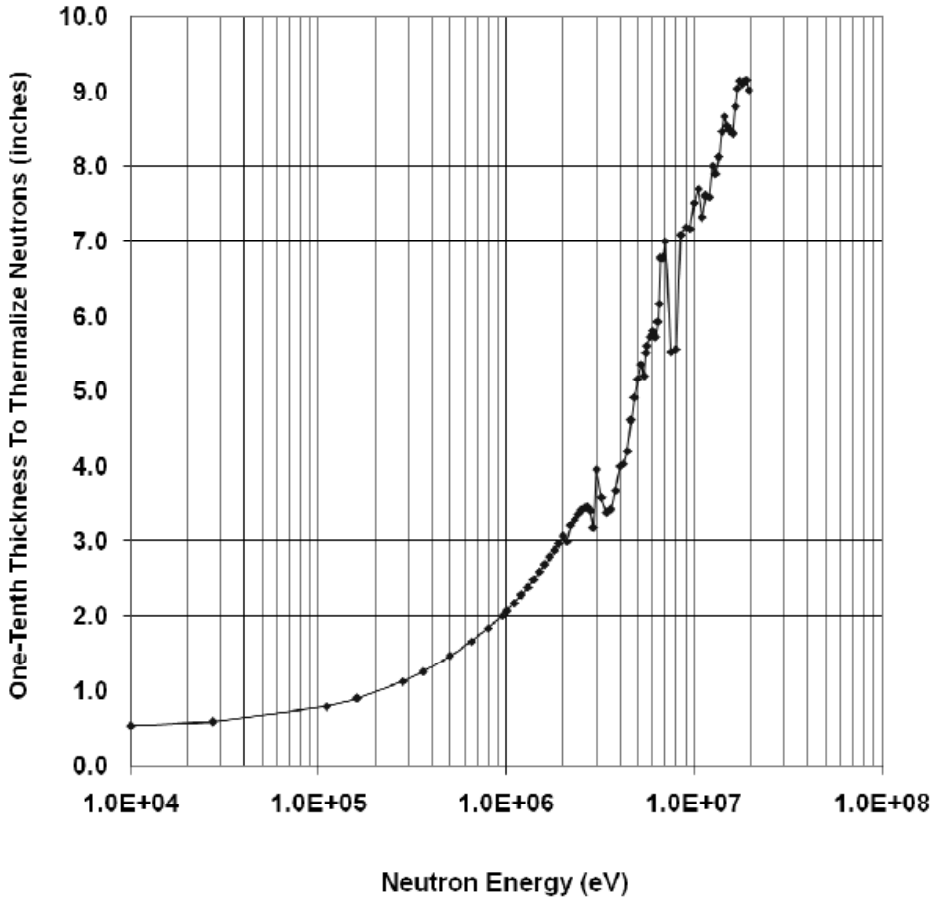


Figure 3.3: This plot was supplied by a polyethylene manufacturer, Shieldwerx, to determine the thickness needed to reduce the neutron flux by a factor of 10. The y-axis displays the thickness needed at a certain energy to get the appropriate reduction.

neutron flux reduced by a factor of 10. The x-axis shows the energies of the incoming neutrons. The y-axis shows the thickness (in inches) needed at a particular energy to get the factor of ten reduction. For example, to block out 10 MeV neutrons sufficiently a shield would require 8 inches of polyethylene. Keep in mind that the theoretical calculations in this thesis are integrated over a range of energies, while the manufacturer's plot looks at thicknesses based on a particular incoming energy. A simple comparison between the three calculations for the energy range of 1-10 MeV is show in Table 3.1. If the energy ranges for the spectrums are restricted to 1-4 MeV, very similar results are produced. Note that for the Shieldwerx values, the 2 in/5 cm value corresponds to 1 MeV.

Table 3.1: Shield Thicknesses for 10x Reduction

| | **Energy Range (MeV)** | **Thickness (in)** | **Thickness (cm)** |
|---|---|---|---|
| Soudan MC | 1-10 | 3 | 7.6 |
| Hess | 1-10 | 2.6 | 6.65 |
| Shieldwerx | 1-10 | 2-7.5 | 5-19 |

Comparing the thicknesses from the calculations using the Soudan MC and Hess' spectra to Shieldwerx's calculations, the first two appear to necessitate smaller thickness values. Also, although the energy spectrums range from 1 MeV-10 MeV, the shield analysis is restricted by the recoil energy to look at an incoming neutron energy range of $\sim$ 0.4 - 4 MeV. 4 MeV from Shieldwerx's calculation corresponds to $\sim$ 5 inches. This is slightly larger than the values produced by the theoretical values calculated in this thesis. It appears that at the lower end of the 1-10 MeV range the three sets of values agree better with one another.

## 3.4 Structure

Due to the erratic nature of a neutron's path, it is not sufficient to shield the detectors just from above. When designing the shield structure it was necessary to minimize gaps. This posed problems for shielding the top of the refrigerator because directly above are cryogenic equipment and electronics. There was simply no available even surface to place slabs of polyethylene. Thus, it was necessary to look within the refrigerator to strategically place shielding material. Based on the polyethylene resources available, it was possible to construct a shield with 8 inches (20 cm.) of thickness on all sides (except above). Within the cryostat, 9 layers of polyethylene were situated near the top, known as the baffle (Fig. 3.7). For further coverage, a disk 1.5 inches thick and 4 inches wide was also placed within the inner can that holds the detector structure. This provided some immediate shielding above the detector.

To support the bulk of the shield and provide simple movement around the refrigerator, a rolling platform was designed such that two of these structures would come together to surround

the refrigerator. Once in place, sheets of polyethylene were slipped onto the threaded rods. The designs for the shield platforms can be seen in Figure 3.4. The final assemblage of the polyethylene in the run can be seen in Figures 3.8, 3.9, and 3.10. With 8 inches of polyethylene surrounding all sides of the refrigerator entirely but the top, which itself has some coverage, a factor of 10 reduction in the neutron flux is a reasonable expectation for the shield.

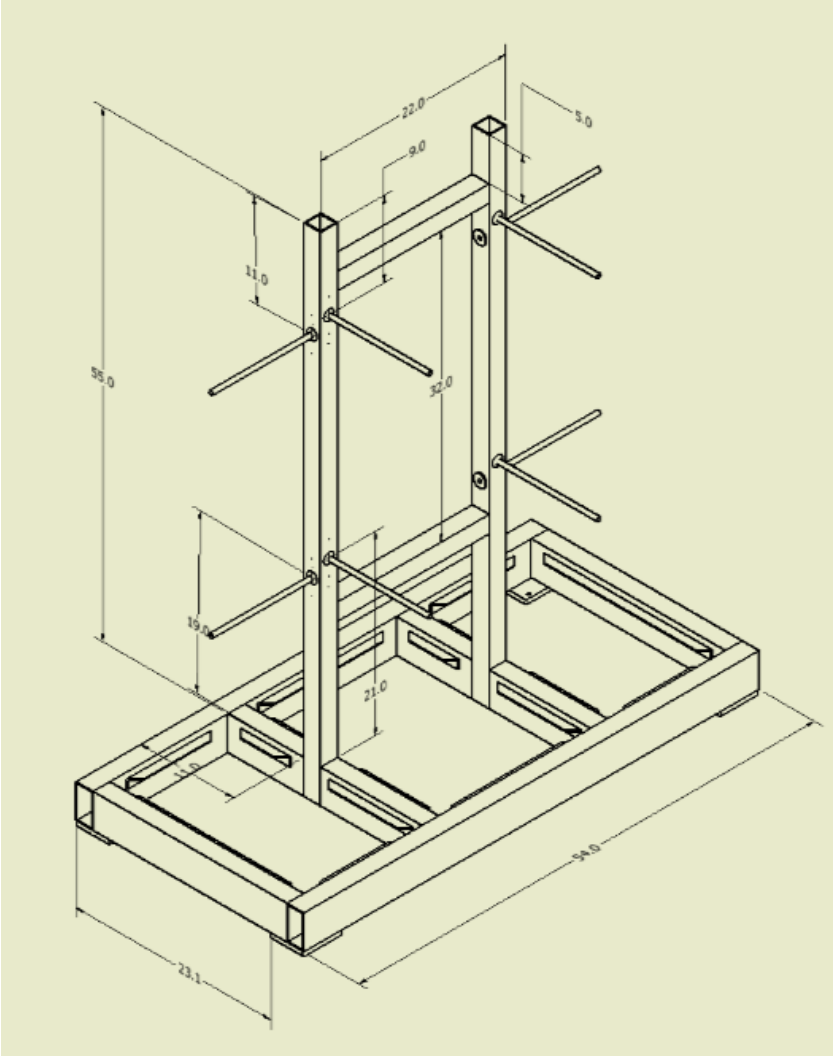


Figure 3.4: The design of the platform which will support the polyethylene structure. Two of these were used to support the outer shield bulk. [32]

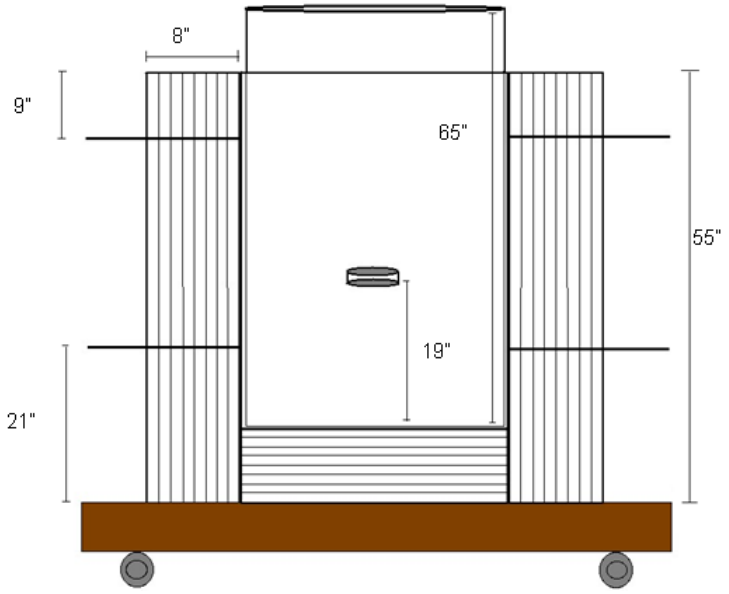


Figure 3.5: A 2-D side schematic with dimensions of the shield surrounding the refrigerator.

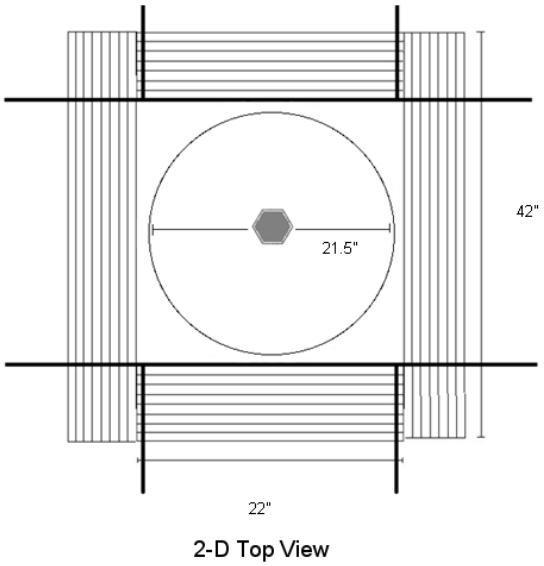


Figure 3.6: A 2-D top view of the shield surrounding the refrigerator.

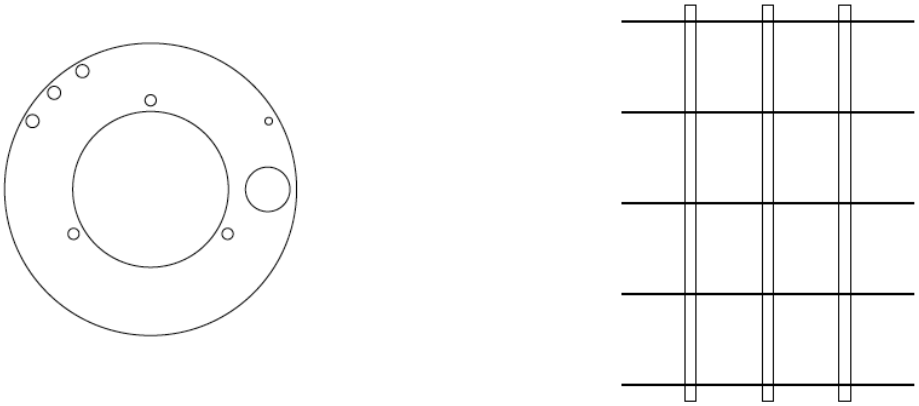

Figure 3.7: On the left is the design for the baffle poly. On the right is a side view of the structure of the baffle itself.

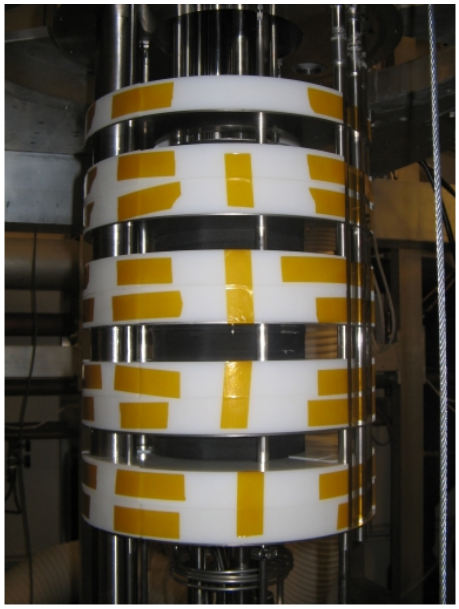

Figure 3.8: A picture of the baffle poly installed. The yellow strips are Kapton tape used to secure the pieces of poly together.

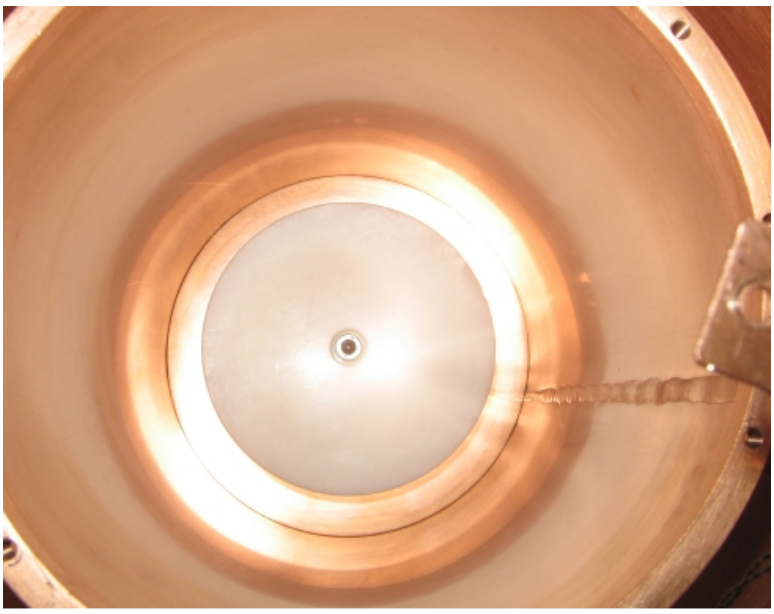

Figure 3.9: Bottom view of the 1.5 inches of poly installed within the inner can (before detector tower is installed).

Figure 3.10: Final assemblage of the neutron shield around the dilution refrigerator.

# Chapter 4

# Analysis

Having constructed the polyethylene shield, the next step is testing the effectiveness of the design by comparing the nuclear recoil event rate before and after the shield is in place. To do this, a detector operating at sub-Kelving temperature was exposed to a neutron source with and without the shield. Using a neutron source will allow more statistics in the analysis, thus making the shielding behavior more distinct.
The iZIP detector, G42, was installed and operated in the UMN dilution refrigerator, K100, with two Am-241 sources positioned directly above the detector (Fig. 4.1). The gamma rays from Am-241 provide a 60 keV reference peak for energy calibration. In addition to these internal sources, the detector was also exposed to external Cf-252 and Ba-133 sources for additional neutron and gamma calibrations. The data from these exposures were analyzed to determine the neutron flux. The following sections describe the analysis procedure and results in detail.

## 4.1 Data Quality Check

Before conducting the analysis of the data sets, data quality checks and correction were conducted. First, an event number cut was made to discriminate noisy data. Then, an energy threshold cut was applied to get rid of low energy events due to noise and zero charge phonon signals. Further cuts were made to remove charge pulse overlaps, surface events on both sides of the detector, and events that took place under the outer charge electrode. Once the cuts were made the final data sets for analysis were properly defined. Table 4.1 shows the total amount of raw data for the shielded and unshielded runs taken with the Cf-252 source. These data sets were used to determine the neutron flux detected by G42. The raw data amount does not reflect any data quality cuts or restrictions on energy range.

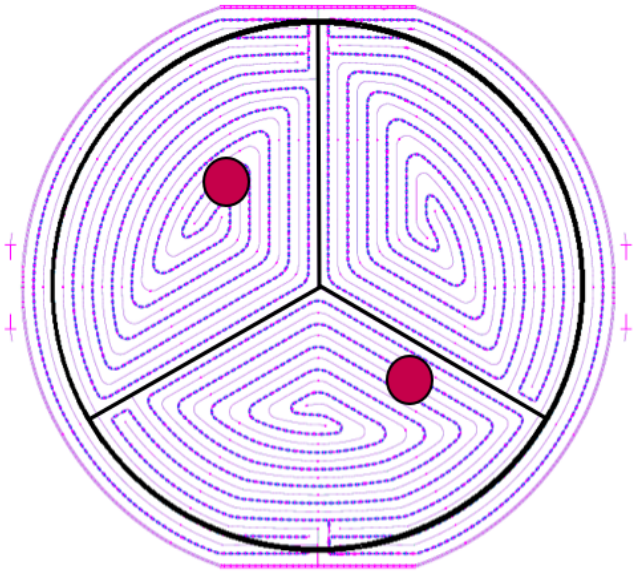

Figure 4.1: The figure shows the phonon (blue, dark) and charge (grey, light) channels interlooping one another. Overlaid on the detector is the simplified layout of the 4 phonon channels (the black circle signifies the boundary for the fourth phonon channel which is a ring). The two small circles represent positioning of the Am-241 sources over the phonon channels.

Table 4.1: Raw data

| **Shield** | **Event Number (counts)** |
|---|---|
| Am-241, Cf-252 | 896607 |
| **No Shield** | **Event Number (counts)** |
| Am-241, Cf-252 | 775421 |

### 4.1.1 Various Noise Rejections

Amongst the first data quality corrections are the analysis of the noise fluctuations in the data collection and the rejection of noise and extremely small charge events that were collected.

#### Noise fluctuations

Events are recorded in the form of charge and phonon pulses. The quality of this data is at the mercy of the behavior of the electronics during acquisition. Thus, it is necessary to check the noise of the data collected to see if there is any distinct noise fluctuation. If such fluctuations are present then the corresponding events must be thrown out. This is the purpose of noise data collection. When a charge pulse is collected (Fig. 4.13), the data acquisition (DAQ) software records a certain amount of noise data before the start of the pulse. This quantity is referred to as the charge baseline. The standard deviation of the charge baseline is calculated for all events in the data sets and then are compared. Plots of the charge noise standard deviation for both data sets can be seen in Figures 4.2 and 4.3. From this analysis, it appears that there is no significant fluctuation in the charge baseline among events that require cuts to be made in the data.

#### Noise and Low Charge Events

Another type of noise occurs at the low end of the charge spectrum. In order for the DAQ software to record events a specific voltage threshold must be placed such that any event which surpasses that threshold triggers a measurement. The lower the trigger threshold, the greater the chance of random noise triggering the measurement. Also, because the triggering occurs on phonon pulses, there is a possibility of obtaining a phonon measurement with a zero charge signal. These events contaminate the data and contribute to a large peak present at the low end of the charge energy spectrum. To reject them, the $Q_i$ signals for each side of detector are filled into a histogram (Fig. 4.4). A gaussian is fitted to each histogram to find the mean value and 3 $\sigma$ is added to that value. This final value becomes the threshold cut that creates a lower limit on the charge energy spectra. The effect of the threshold cuts can be seen in Figure 4.5. This cut is reflected in a charge spectrum quantity that is defined in section 4.1.3. Due to the threshold cut the low energy peak is reduced by at least an order of magnitude.

### 4.1.2 Bulk Events Selection

Recall from Chapter 2 that events occuring near the edge of the crystal need to be rejected. These appear as large signals in the outer charge electrode. To effectively do this a ratio of the difference and the sum of $Q_i$ and $Q_o$ (charge partition) are plotted to identify the events in $Q_i$ (Fig. 4.6):

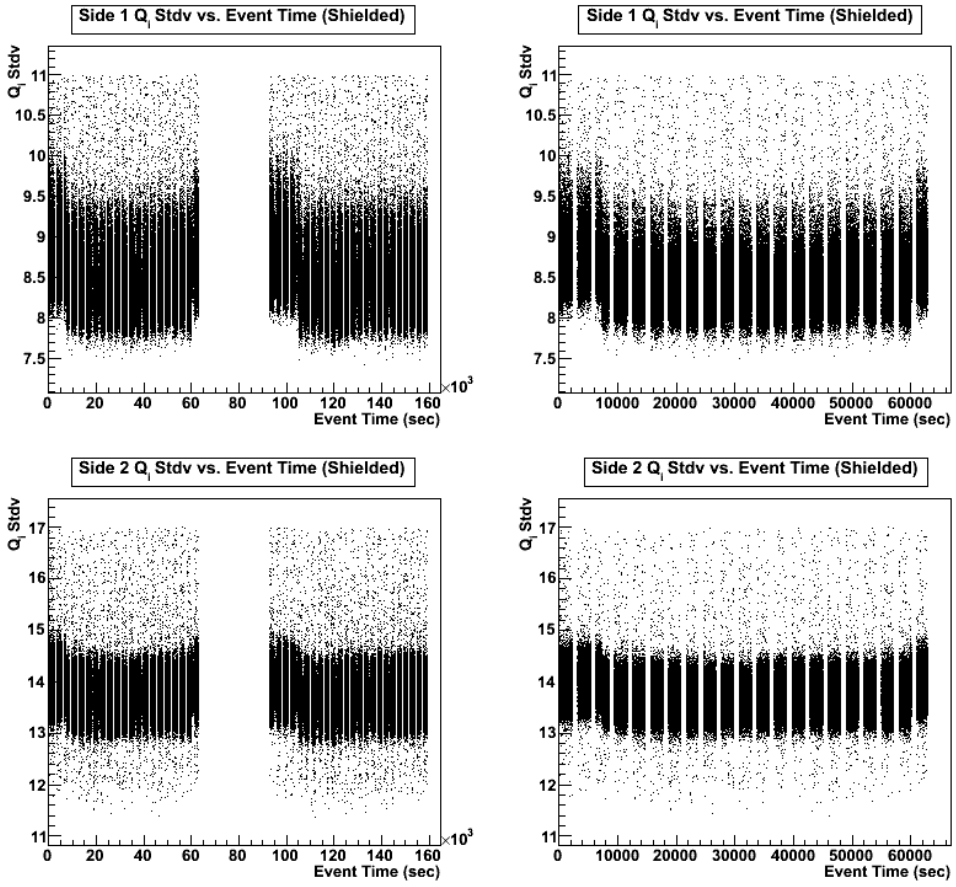


Figure 4.2: Note that for the shielded data sets there are two distinct groups. This is because these two sets were not taken sequentially in time. The same can be said for the unshielded data sets, which were taken at three non-sequential times. The plots in the left hand column are the full data sets. The plots in the right hand column are close-ups of the first data series to get a better resolution.

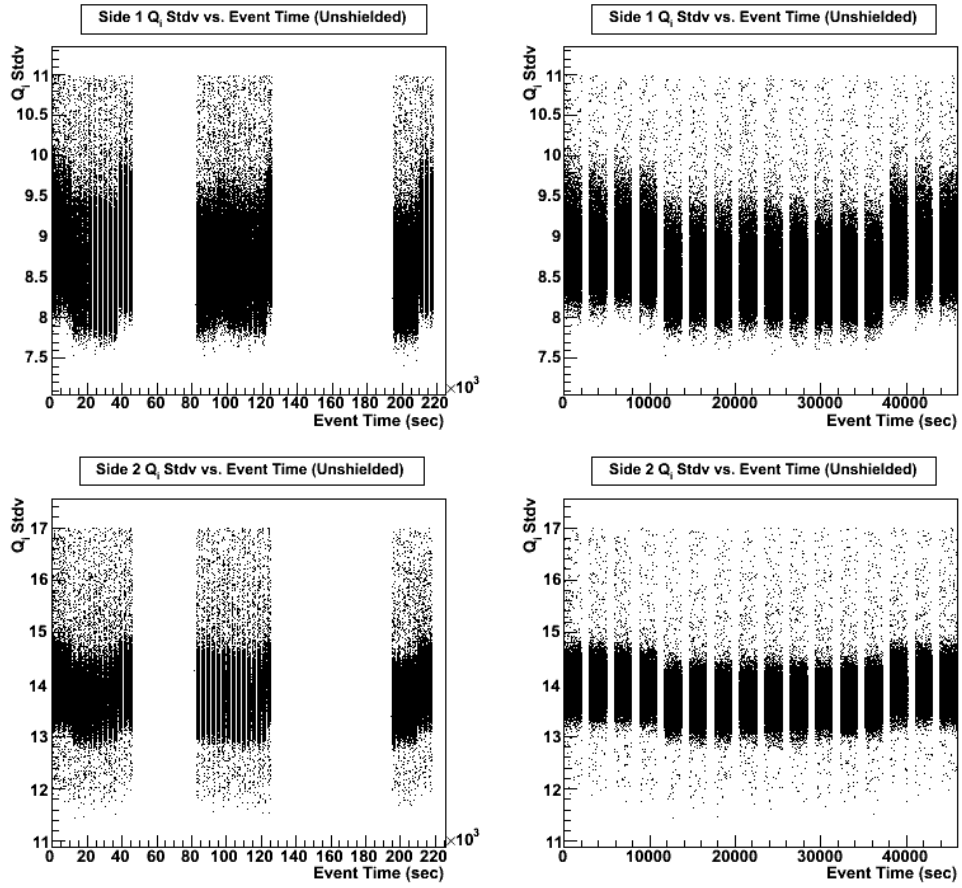


Figure 4.3: Similar to the case of the shielded data (Fig. 4.2), the unshielded data sets were taken at three non-sequential times. The plots in the left hand column are the full data sets. The plots in the right hand column are close-ups of the first data series to get a better resolution.

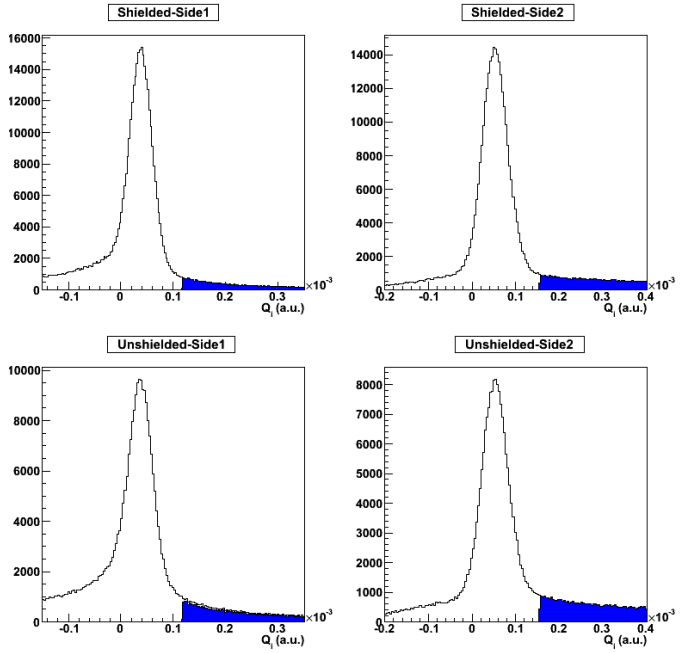


Figure 4.4: The peaks above represent the large low energy peak due to noise and zero charge events. A gaussian is fitted and $+3\,\sigma$ cut is placed to act as a lower limit on the charge spectrum.

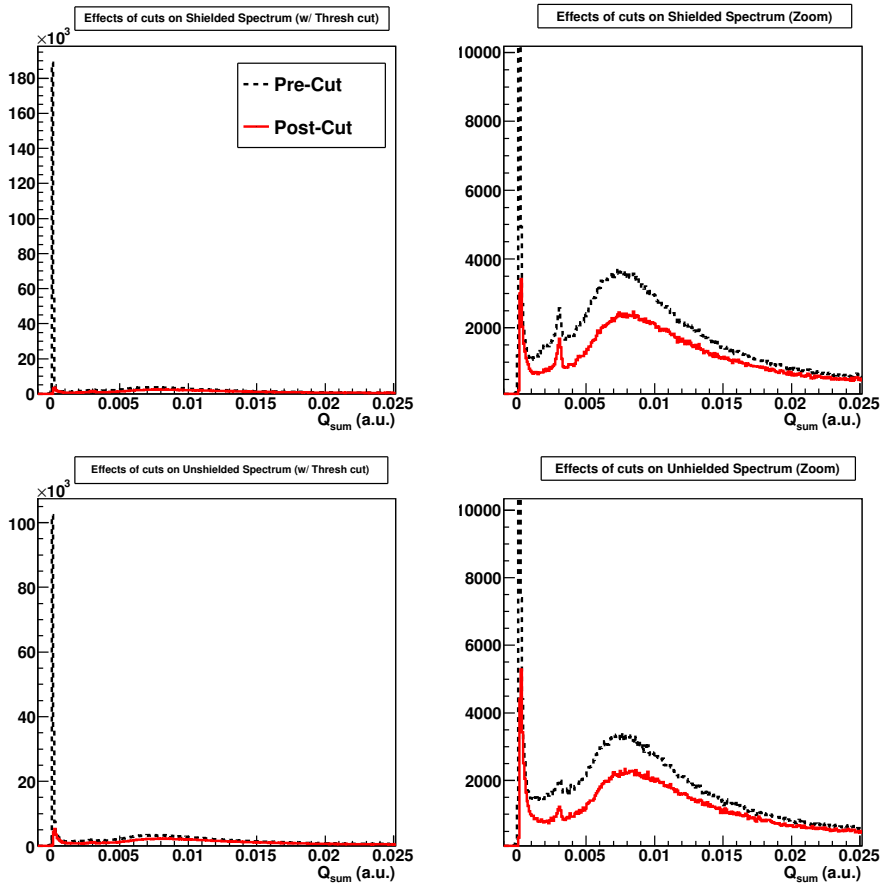


Figure 4.5: Comparison of charge spectra (arbitrary units) with and without the threshold cut for the shielded and unshielded data sets. The figures on the right zoom in on the low energy peak. The large spike in the left-hand figures correspond to the peak fitted in figure 4.4. Note that the charge spectrum $Q_{sum}$ is defined in section 4.1.3.

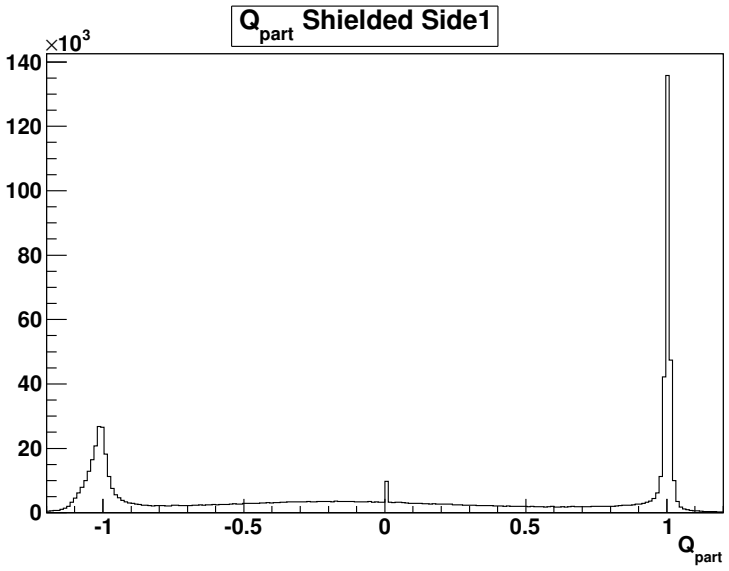


Figure 4.6: Distribution of charge signal dominance in inner and outer electrodes.

$$Q_{part,\#} = \frac{Q_{i,\#} - Q_{o,\#}}{Q_{i,\#} + Q_{o,\#}} \tag{4.1}$$

where # refers to the side of the detector since $Q_{part}$ is being calculated for each side of the detector.

It is expected that events occuring in the bulk of the crystal to correspond to a $Q_{part} = 1$. Figure 4.6 supports this by displaying a dominance of $Q_i$ events at $Q_{part} \sim 1$ (Fig. 4.6). Likewise, a dominance of $Q_o$ events should occur at $Q_{part} \sim -1$ . Figure 4.7 shows the $Q_i$ peaks of both sides of the detector for the two data sets. A gaussian fit is applied to the peak at 1 and a cut is made around the mean value +/- 3 $\sigma$ to keep only events within the peak. This will be used in the analysis as the bulk event cut. However, this is not quite sufficient in keeping out events near the detector edge. Thus, a study of $Q_o$ will be made as well.
Using the bulk event cut from $Q_{part}$, $Q_o$ (from both sides of the detector for the two data sets) is filled into a histogram and fitted with a gaussian. A selection of zero charge $Q_o$ events is made based on limits determined from the mean value of the peak +/- 3 $\sigma$. This $Q_o$ selection coupled with the bulk event cut places a more stringent cut against the number of events occurring near the edge of the detector. In turn, this combination of cuts helps identify true bulk events for the analysis.

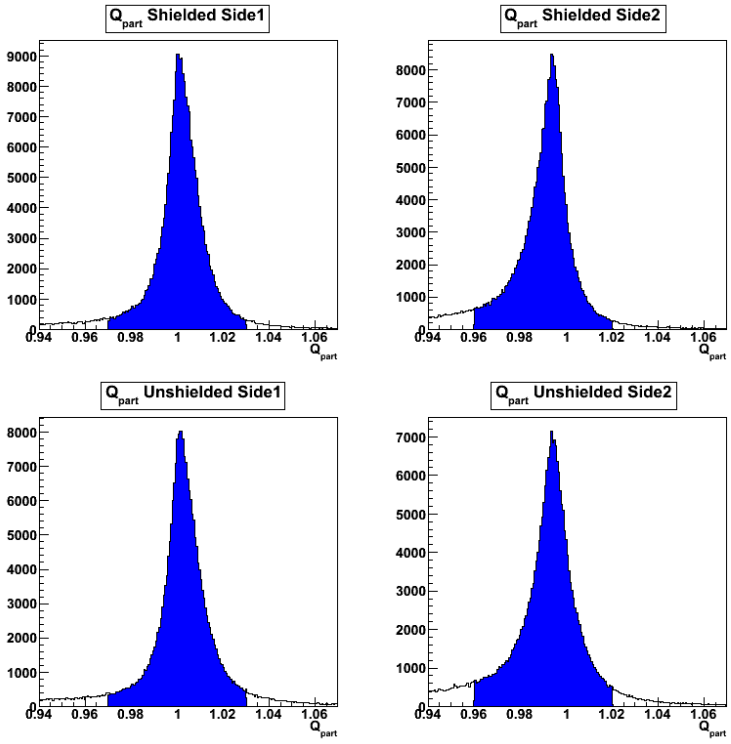


Figure 4.7: Distribution of charge signal dominance in inner electrode. Events within the shaded region are represent a selection of the peak's mean value $\pm$ 3 $\sigma$.

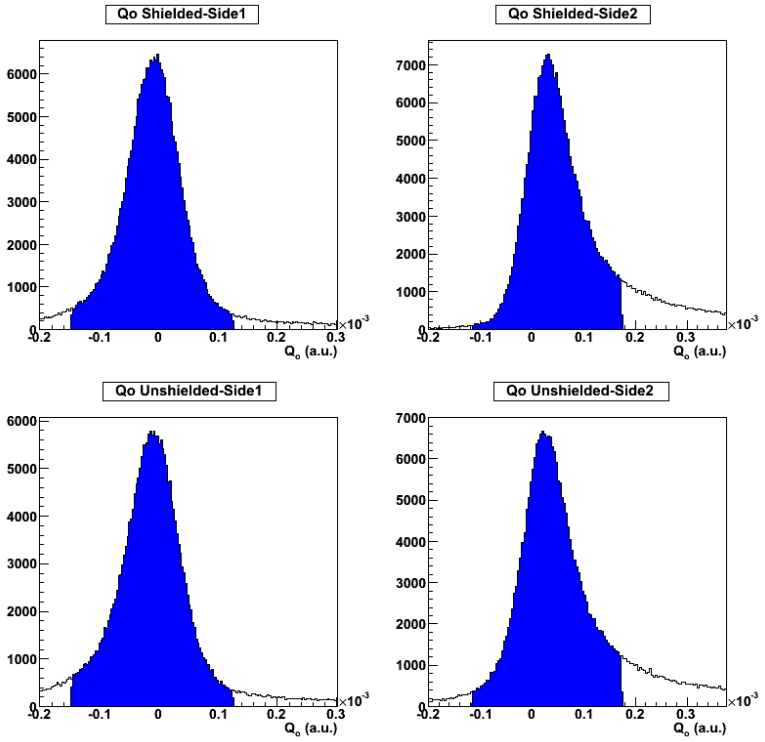


Figure 4.8: $Q_o$ events are rejected that fall $\pm$ 3 $\sigma$ outside of the mean value of these peaks.

### 4.1.3 Surface Events Rejection

An appealing feature of the iZIP detectors is their capability reject surface events effectively. One of the reasons for this is the presence of charge electrodes on both sides of the detector. Events that have significant ionization signals on both sides of the detectors are took place in the bulk of the crystal. To determine these symmetric events two plots are studied: a charge partition incorporating both sides of the detector, and a scatter plot of one detector side's charge energies versus the other side. The charge energy quantities are a combination of $Q_i$ and $Q_o$:

$$Q_{sum,\#} = Q_{i,\#} + Q_{o,\#} \tag{4.2}$$

The two-side charge partition $Q_{zpart}$ $(QZ)$ is defined as:

$$Q_{zpart} = \frac{Q_{sum,1} - Q_{sum,2}}{Q_{sum,1} + Q_{sum,1}} \tag{4.3}$$

where $Q_{sum,1}$ and $Q_{sum,2}$ refer to side 1 and side 2, respectively, for each data set.

There is a double peak feature in the $Q_{zpart}$ plot (Fig. 4.9). There is a slight split in $Q_{zpart}$ over time, but the cause of this split is not fully understood (Fig. 4.10). Because the split was small, a cut on $Q_{zpart}$ was placed around the edges of the double peaks at $\sim$ -0.1 and 0.1 to reject events outside this range. To see the effect of the cut it was applied to a scatter plot of $Q_{sum,2}$ and $Q_{sum,1}$ (Fig. 4.11). The thick band in the center are the events with symmetric charge energies on the two sides of this detector and the cut based on $Q_{zpart}$ effectively selects that band of events. Thus, even though there is a slight split in $Q_{zpart}$ and the source for this is unconfirmed, the analysis will probably not be affected negatively to a significant degree.

$\underline{Q_{sum}}$

A new quantity for the charge spectrum will be used that combines the charge quantities from both sides of the detector. When the signals from both sides of the detector are combined together, the maximum signal between the two sides will be selected. A comparison of $Q_{sum,2}$, $Q_{sum,1}$, and the maximum of the two combined can be seen in Figure 4.12. The black curve represents the maximum of the two sides which will be known from now on as $Q_{sum}$:

$$Q_{sum} = \max\left(Q_{sum,1}, Q_{sum,2}\right) \tag{4.4}$$

This quantity is used in standard CDMS analysis.

### 4.1.4 $\chi^2$ Cut

The $\chi^2$ cut is a quality cut that eliminates charge pulses poorly fit during data processing. This cut is applied after the charge energy calibration (which will be discussed further in the

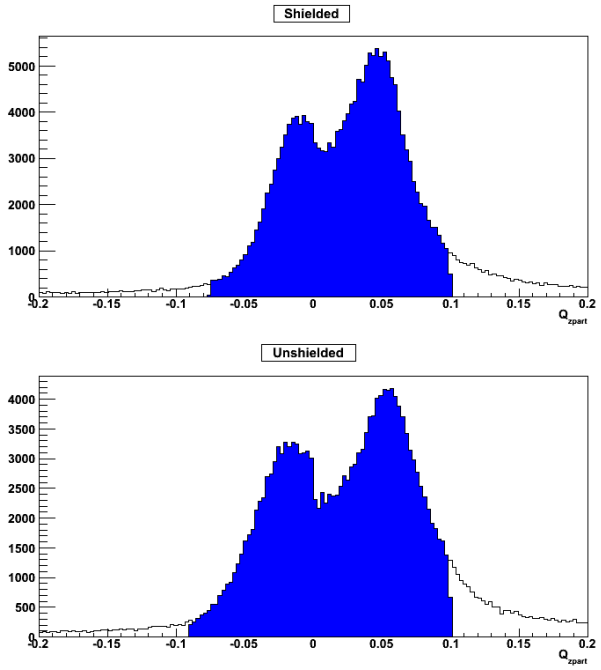


Figure 4.9: Distribution of charge signal dominance in $Q_{zpart}$.

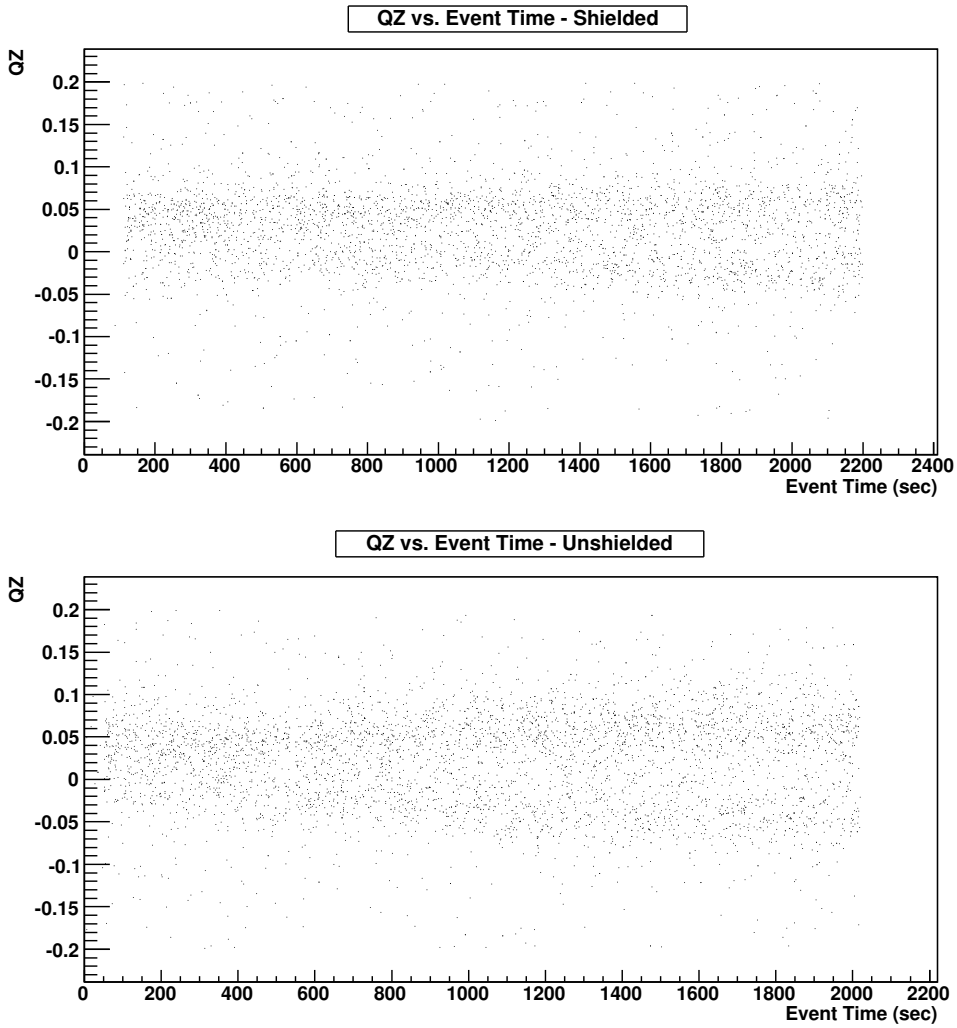


Figure 4.10: $Q_{zpart}$ vs. event time in the first series of each data set. There is a slight split in the events that becomes noticeable around 700-800 seconds.

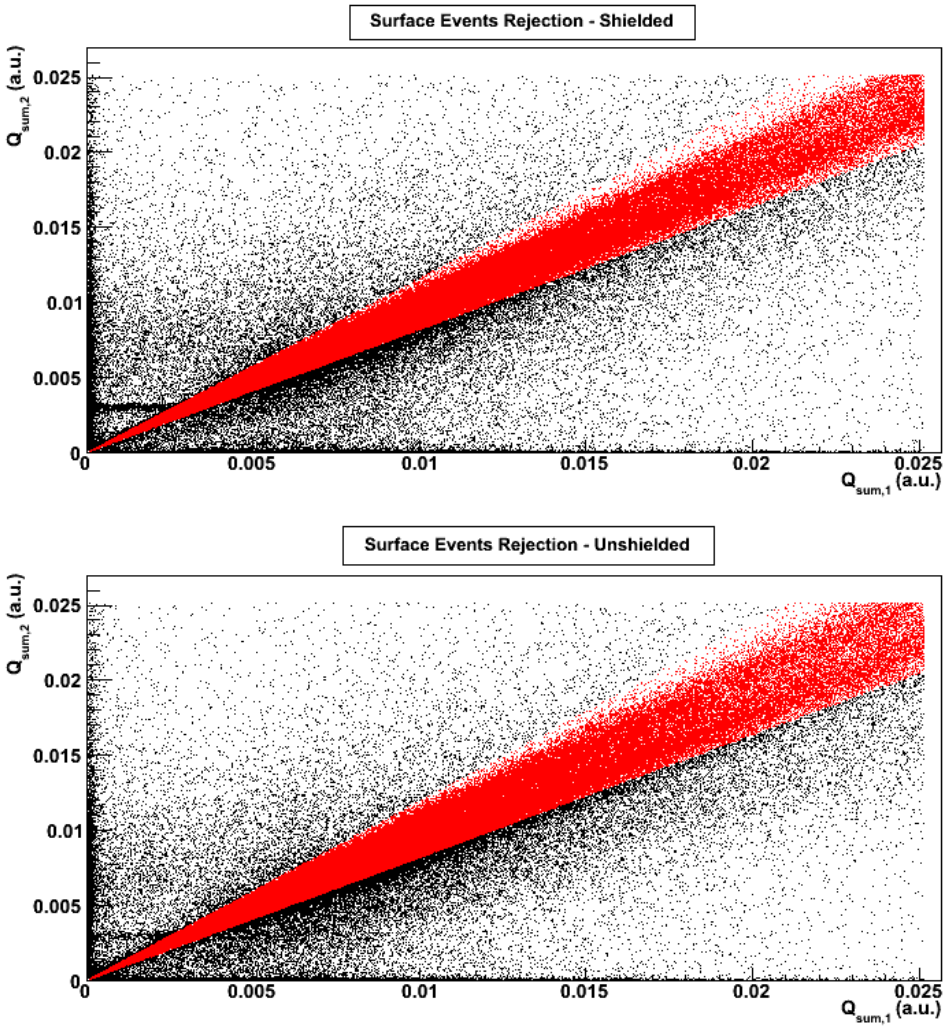


Figure 4.11: This figure displays the selection of symmetric events between $Q_{sum,1}$ and $Q_{sum,2}$. The cuts applied to this figure to obtain the black events are the threshold cut and the combined $Q_i - Q_o$ bulk cut. The red events are those that pass the surface event rejection cut. Note the horizontal lines on the $Q_{sum,2}$ axis at the value 0.003. This line represents the events from the Am-241 sources not occurring within the bulk of the detector. Because the internal sources were placed on side 2, the 60 keV line is quite distinct. Side 1, however, does not have a good signal for 60 keV surface events.

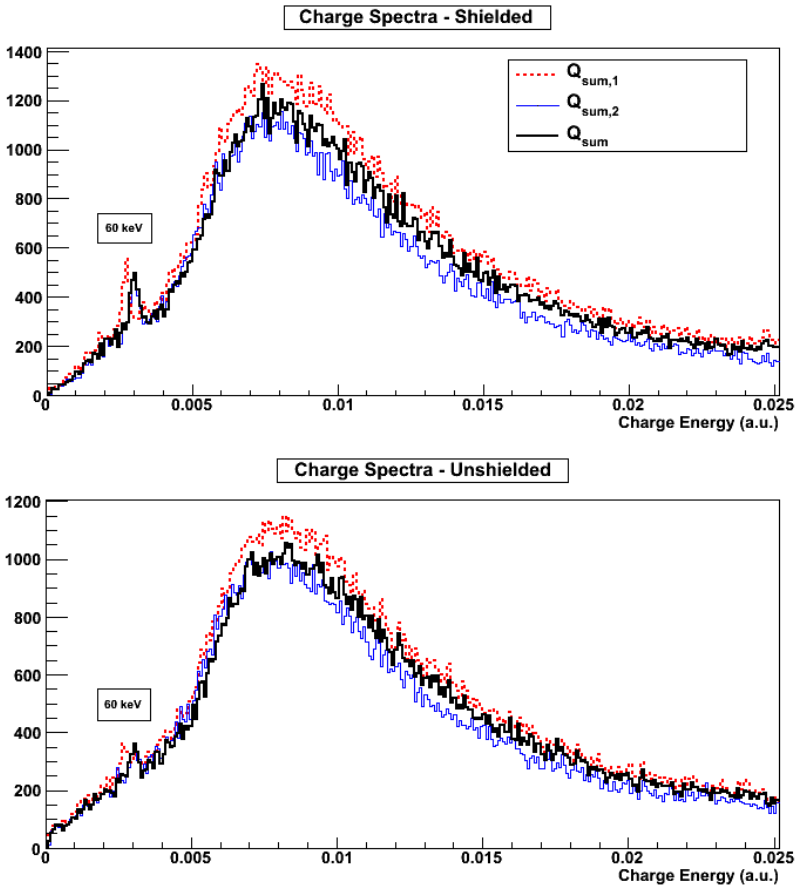


Figure 4.12: This is a comparison of the uncalibrated (thus with arbitrary units) $Q_{sum,1}$, $Q_{sum,2}$, and $Q_{sum}$ spectra. Once calibrated, $Q_{sum}$, which takes the maximum value from the combination of $Q_{sum,1}$ and$Q_{sum,2}$, will be used in the phonon calibration and yield vs. phonon energy analysis. The 60 keV peak noted in the spectra is due to the internal Am-241 sources.

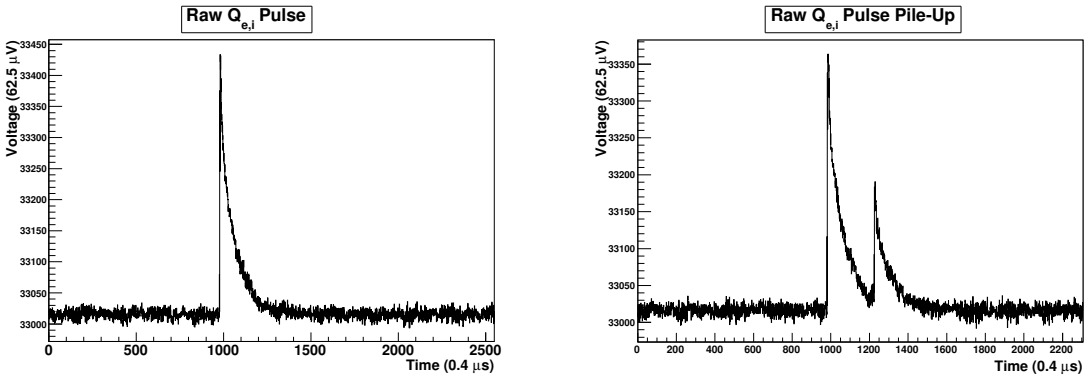


Figure 4.13: a) A raw charge pulse. This is an example of a pulse that is fit by a pre-defined function in CDMSBATS. The rise time should be 1 $\mu$s and the attenuation time is 40 $\mu$s. b) An example of a charge pulses piling up on one another, which results in a poor fit on the pulse.

next section). When charges are detected their pulses are recorded by the DAQ software (Fig. 4.13a). A standard CDMS analysis package, CDMSBATS, fits a predefined function to the charge pulses, and produces a measure of the quality of the fit known as the $\chi^2$. This quantity is then plotted against the charge signal amplitude, in order to identify events with poor fit quality.

A thick band of events follows a parabolic curve with a dominance of background events occurring at low energy and $\chi^2$ (Fig. 4.14). There is a scattering of events above that band that need to be cut out. Some of these events represent an overlap of charge pulses collected (similar to that seen in Fig. 4.13b ) when the detector is inundated by these pulses. The pre-defined function from CDMSBATS does not fit pulses that pile up effectively which are identified through the use of the $\chi^2$ values. It is important to reject these events during the process of data quality correction. Thus, a $\chi^2$ cut is applied after the charge energy calibration. To define this cut, a polynomial $a * x^2 + b * x + c$ is fit right above the thick curve of events (Figs. 4.14). All events below the polynomial, indicated by the red band, pass the $\chi^2$ cut.

### 4.1.5 Final Data

The final event number is a result of all of the above quality cuts with no specified energy range (Table 4.2). When looking at the reduction of neutrons in the shielded versus unshielded data, the fact that there was more data in the shielded data set (due to longer exposure) must be taken into account. To determine the scaling factor, several ratios were calculated based on different energy cut-offs (Table 4.3). This was done to see if the ratio of the two data sets were more consistent at higher energies where the shield would have less of an effect on the flux of the

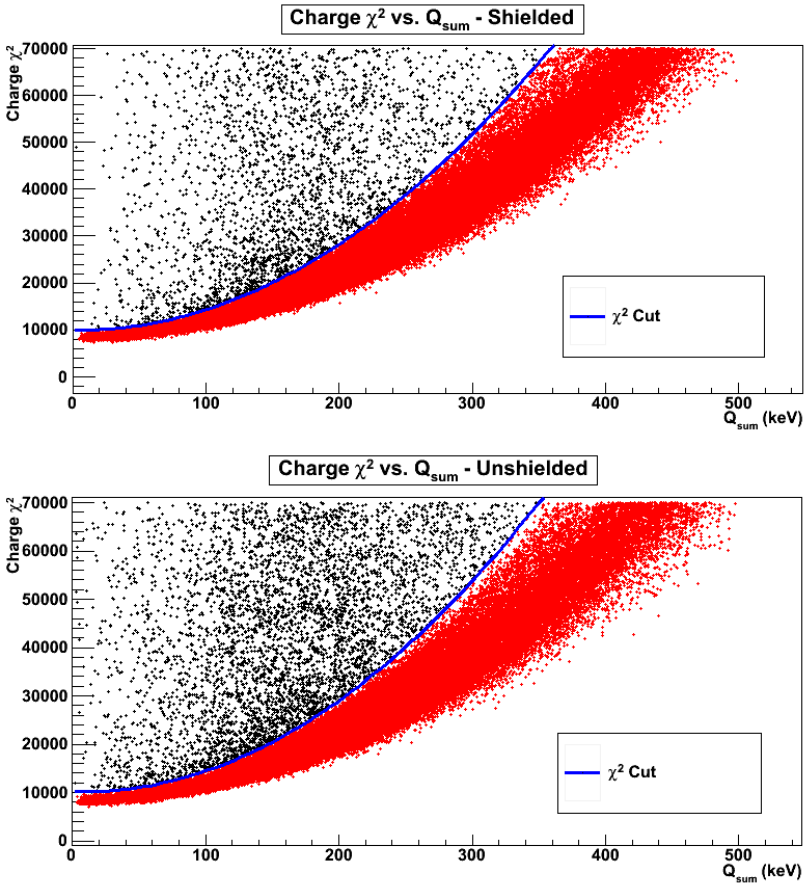


Figure 4.14: All previously discussed cuts are implemented for this plot. The red band signifies the events passing the cut line, represented by the line following the parabolic curve.

particles hitting the detector. Based on the values in Table 4.3, the count for the shielded data set will be scaled to match the unshielded set by dividing the shielded set by 1.10. Choosing the smallest scale factor will place an upper limit on the shielding effect in the analysis.

Table 4.2: Final data after all cuts

| **Shield** | **Event Number (counts)** |
|---|---|
| Am-241, Cf-252 | 169783 |
| **No Shield** | **Event Number (counts)** |
| Am-241, Cf-252 | 138807 |

Table 4.3: Ratios of the two data sets to determine scaling factor

| **Energy Cut-Off** | **Scaling Factor** |
|---|---|
| No cut-off | 1.22 |
| 300 keV | 1.15 |
| 700 keV | 1.10 |
| 1100 keV | 1.19 |

## 4.2 Charge and Phonon Energies Calibration

When the data collected is processed, the charge and phonon energies are in arbitrary units (a.u.). In order to calibrate these spectra properly, a distinct feature in the energy spectra is needed as a reference. The Am-241 sources have a 60 keV peak which will be used for this purpose. In the $Q_{sum}$ energy spectrum (Fig. 4.12) the 60 keV line is a distinct spike at $\sim 0.003$ (a.u.). A gaussian was fitted to this peak and a conversion factor was found to put $Q_{sum}$ in appropriate units of keV (Fig. 4.15).

Recall that both the phonon and the charge channels measure the energies of the events. The phonon channels should be calibrated such that their energy responses for electron recoils are equivalent to the charge energies for the same events. Thus, the 60 keV peak could again be used as a reference. However, another method of calibration can be performed with the 60 keV source as a check. When comparing $Q_{sum}$ to the total phonon energy from all 8 channels ($P_{tot}$) there is a diagonal band of events that has a slope less than 1(Fig. 4.16). This main band consists of the electron recoil events due to gammas. To calibrate these electron recoils such that the charge and phonon energies are the same the diagonal band must have a slope of 1. Rescaling the phonon energies to achieve this slope, one can see in Figure 4.17 that the 60

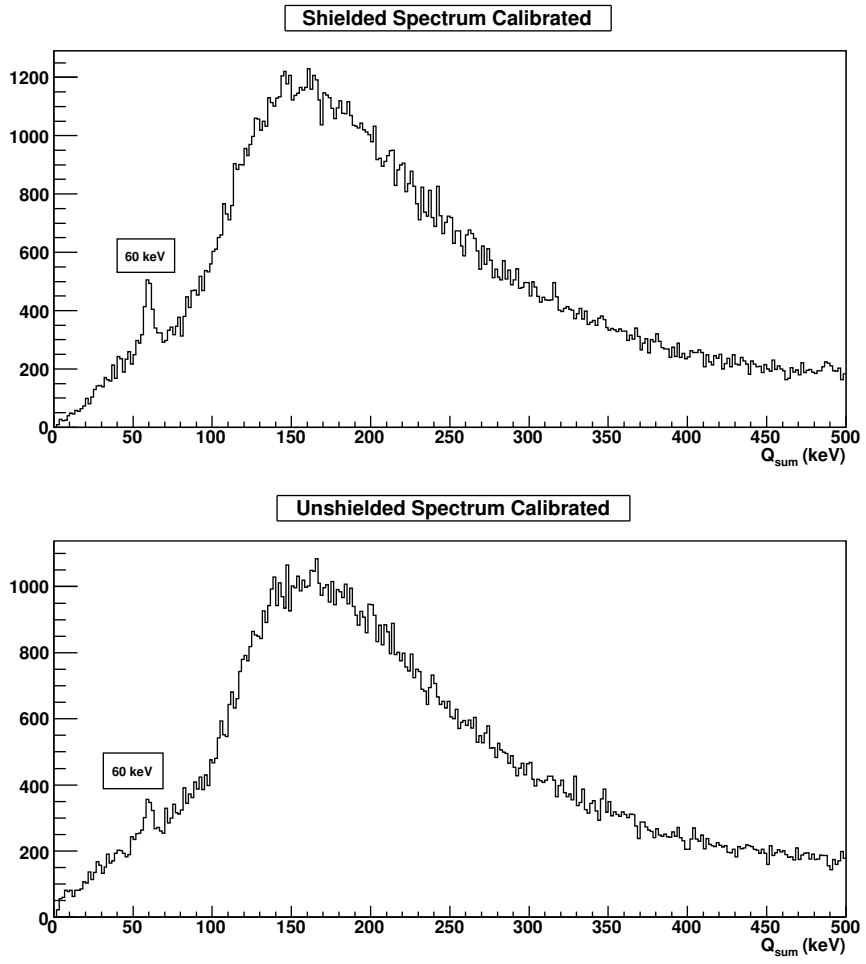


Figure 4.15: These are the final calibrated $Q_{sum}$ energy spectra for both data sets.

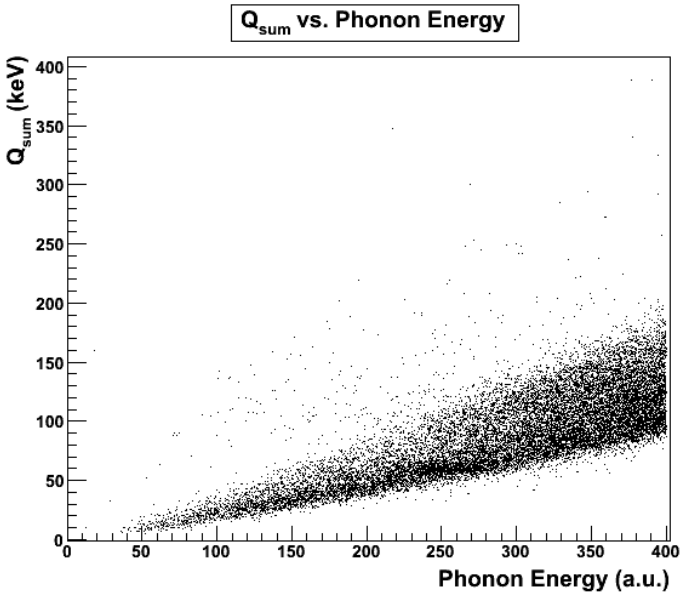


Figure 4.16: This is a figure of $Q_{sum}$ vs. phonon energy that is uncalibrated. The 60 keV gammas can be seen at the value of 250 on the phonon energy axis and at 60 keV on the $Q_{sum}$ axis. This will be used as a reference later. Because the band is projected at an angle less than 45 degrees, this implies that the phonon energies must be scaled down to obtain a slope of 1.

keV source lies roughly above 60 keV on the phonon energy axis (the source is much fainter in the unshielded data set). It is important to make sure that the phonon energies in both data sets are calibrated in the same way. If the phonon energies are not calibrated properly, then the size of the electron recoil bands in the shielded and unshielded data sets will differ, which will negatively affect the shield analysis. Thus, two checks can be made to prevent this. One check is to plot the events from the two data sets on top of one another (Fig. 4.18). It appears that the bands and sources rougly cover one another, which is a good sign. The other check is to look at the $Q_{sum}$ spectrum over a short range of phonon energies and see if the spectrums have similar behaviors at the same energies (Fig. 4.19). This check also confirms that the two data sets have been calibrated properly.

## 4.3 Yield vs. Phonon Energy

In typical CDMS analysis the yield is defined as the ratio of charge and recoil energies. However, for this analysis the yield will be defined as the ratio of charge and phonon energies. This quantity is used to distinguish electron and nuclear recoils, the latter contributing to low yield events

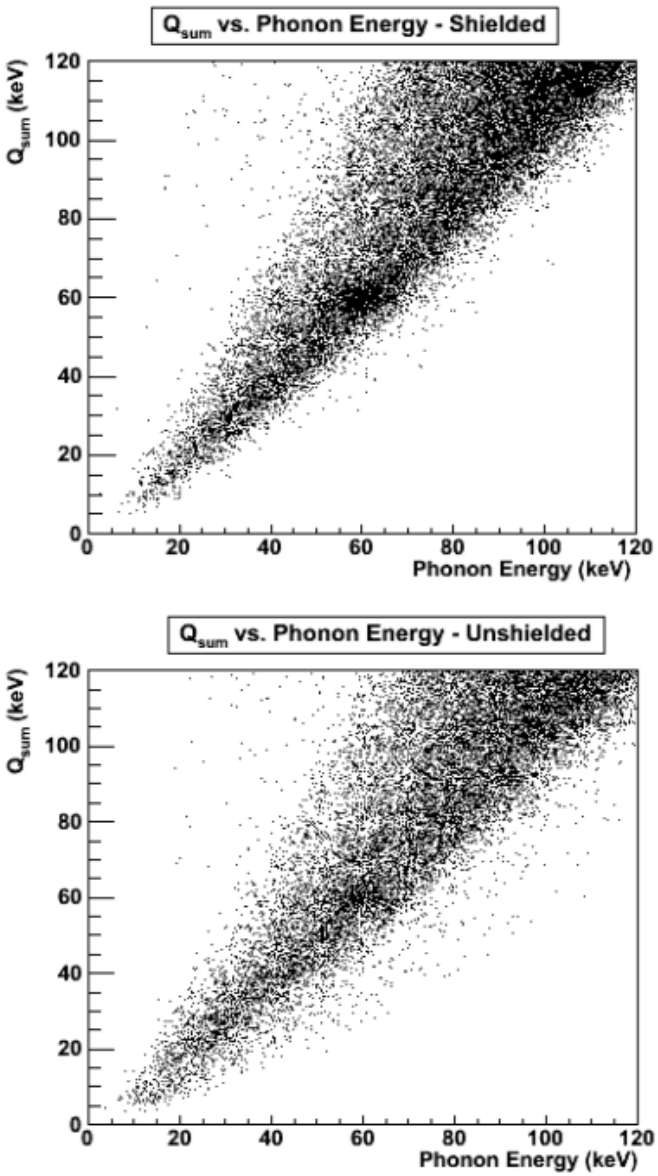


Figure 4.17: These plots show $Q_{sum}$ vs. the calibrated phonon energies. As a check of the calibration, one can look at the 60 keV source and find that it is aligned along each axis properly.

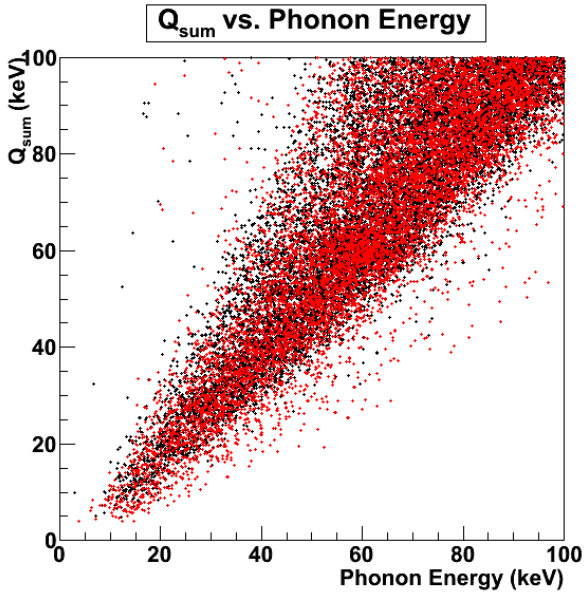


Figure 4.18: One check to confirm that the phonon energies in both data sets were calibrated consistently, they can be plotted over one another. If they fall over one another sufficiently in the same energy range, then this supports the calibration performed, which this figure suggests.

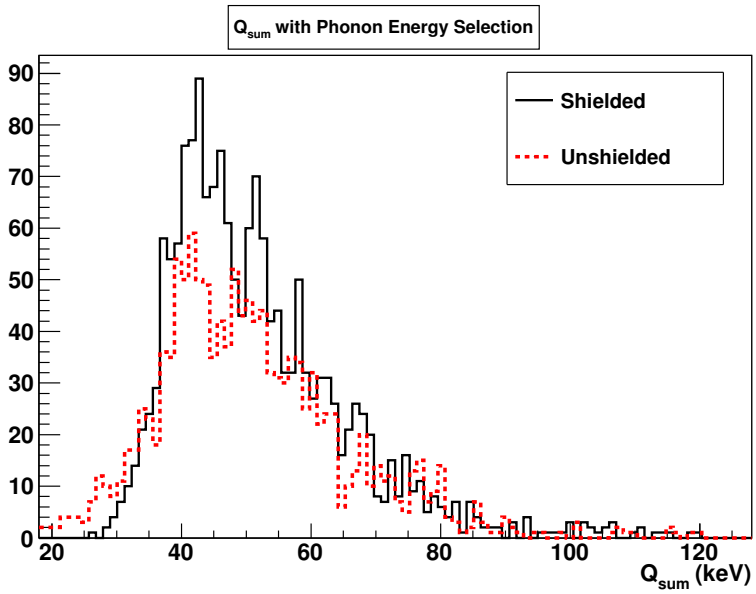


Figure 4.19: Another check to make sure that the phonon energies for the shielded and unshielded data sets were calibrated similarly. $Q_{sum}$ was histogrammed with a selection of phonon energies from 40-50 keV. The peak for both data sets are located at the same $Q_{sum}$ value, which confirms that the calibrations of the two data sets are consistent.

due to their reduced ionization signal. A look at the individual yield versus phonon energy plot for each data set can be seen in Figure 4.20. Due to the calibration of the phonon energy the electron recoil band consisting of gammas is concentrated around a yield value of 1. The unshielded data indicates a larger population of events in the yield range of 0.2 - 0.5, which are expected to be nuclear recoil events due to neutrons from the Cf-252 source. To compare more effectively, the two plots are overlaid with the unshielded data highlighted in red in order to make a better distinction between the two data sets (Fig. 4.21). The greater density of nuclear recoil events in the unshielded data is apparent. Unlike the yield versus recoil energy plot in Chapter 2 (Fig. 2.6) there is no clear distinction between an electron recoil band and nuclear recoil band. This could be due to the fact that there was no correction for the variation in detector response across the detector. To quantify the effect of the neutron shield, a population of nuclear recoil events in both data sets needs to be defined. This will be discussed in the following section.

## 4.4 Shield Results and Implications

Due to the fact that there isn't a clear distinction between the different types of recoils, various cut-offs will be made in the yield plot to mimick designating regions of different sizes that contain nuclear recoils. One example can be seen in Figure 4.22. A line of slope 2.2e-3 was created to run parallel along the lower edge of the dense region of events. The y-intercept, to be referred to as the neutron selection parameter (NSP), is chosen to be at a value of 0.55 (for the sake of the example). The nuclear recoil events are defined to be events below this line and above the yield = 0 line. With this definition, a count can be made for the number of events left in the shielded and unshielded data sets within the phonon energy range of 10-100 keV and ratio of their respective counts will provide the reduction factor due to the neutron shield. To see the effect of changing the region of designated nuclear recoils the NSP value is varied from 0.2 to 0.75 (an upper limit where it is clear from the yield plots that the cut is entering a region of electron recoil events). A plot of the ratio of shielded to unshielded events vs. the NSP can be seen in Figure 4.23. Notice how the lowest value of the NSP plot is actually at 0.41. This is due to the fact that there were zero shielded events in the yield plot below the NSP value of 0.41. Note that the shielded data set was scaled down appropriately such that both data sets had the same amount of exposure (Table 4.2).

Figure 4.23 shows a continuous increase in the ratio as the NSP value increases. This makes sense because a higher NSP means cutting into the region with higher numbers of electron recoils. Since the shield is expected to block out neutrons mostly, it is not surprising that the counts between the two data sets become comparable when including the high-yield region. The rate of increase in the ratio is not constant, though. In the boxed region of low NSP values there is a low gradient trend at a ratio of $\sim 0.08$. The behavior within the box is signficantly

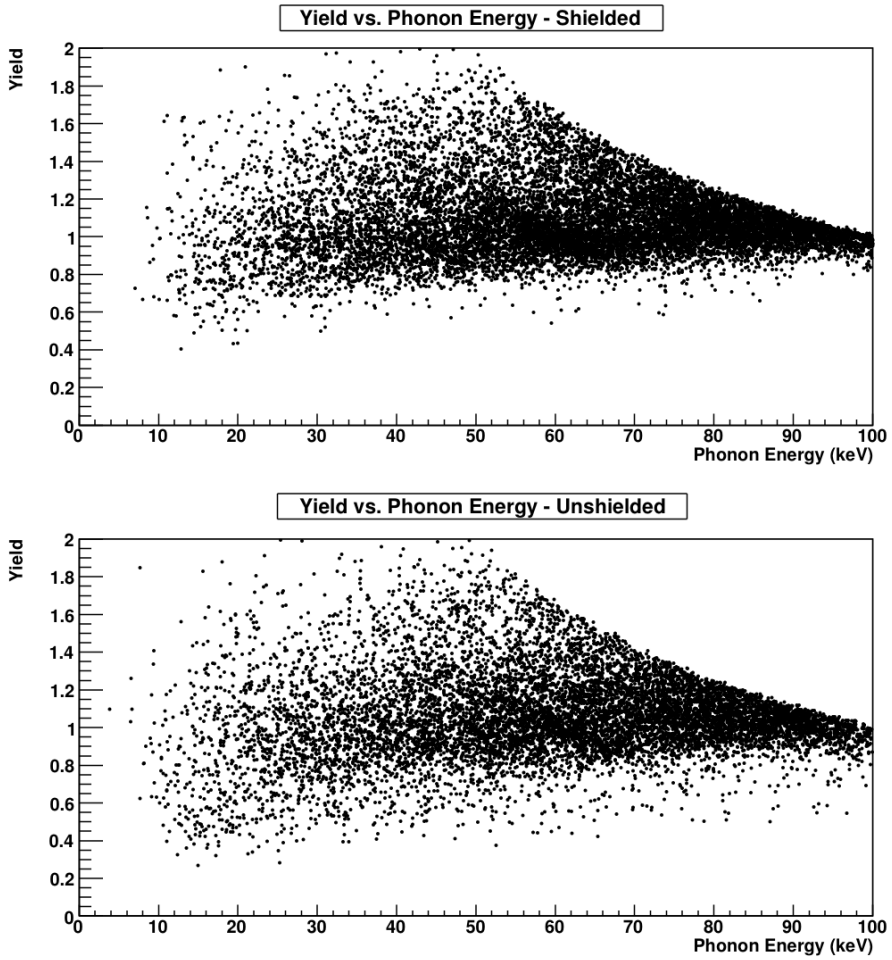


Figure 4.20: Yield (defined as $Q_{sum}/P_{tot}$) vs. $P_{tot}$. The sharp upper curve is due to the restriction of $Q_{sum}$ to the range 10-100 keV.

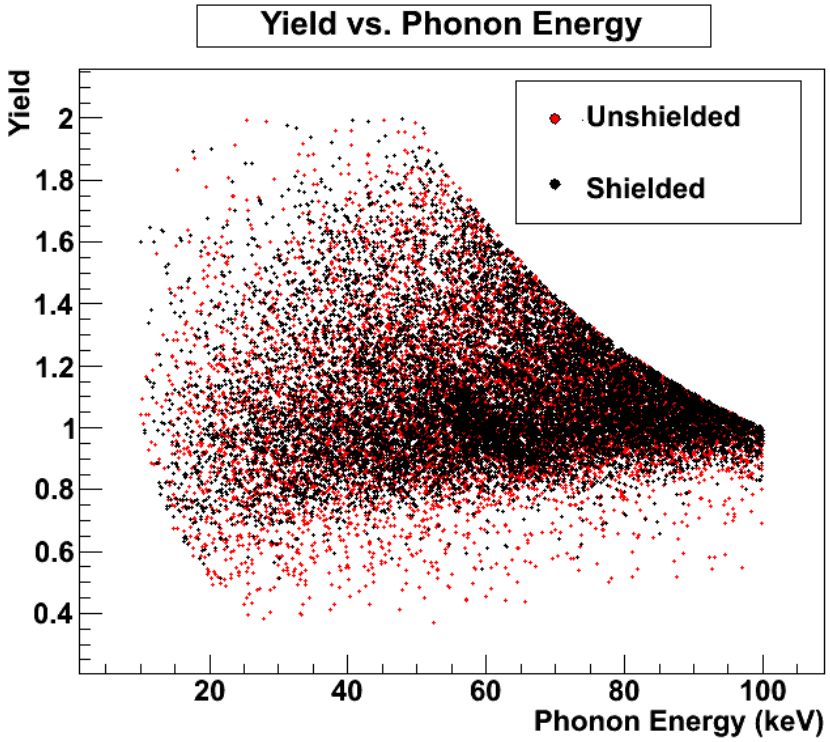


Figure 4.21: Overlay of yield vs. $P_{tot}$. The larger number of red events below the yield value of 0.55 suggests that there is some shielding effect taking place. A count of these events will be made to determine the ratio of shielded to unshielded nuclear recoil event rates.

different from the NSP values beyond 0.55. After the NSP value of 0.55, a distinct increase in the ratio begins to occur. Looking back at Figure 4.21 one can make the connection that at 0.55 the cut begins to encroach on the line where the density of events due to electron recoils increases significantly.

Recall from Chapter 3 that the expectation of the neutron shield was to reduce the neutron flux by a factor of 10 (Table 3.1). The results from the shield tests suggest that a reduction of factor $\sim 10$ or better occurred. This first shield test with an iZIP detector has demonstrated very promising results. To confirm or dispute these results more tests with the shield should be taken with different iZIP detectors. Determining a consistent shielding factor will be very useful when characterizing detectors.

CDMS is continuously progressing its detectors and equipment, and because the UMN group runs an R&D facility much of the technology they use is still under development and testing. Thus, there are several aspects to consider for this work that may have played a significant role in the results. For example, this was the first time G42 has ever been tested. Because the UMN facility is the first to take data for this detector the performance of this iZIP has not been well studied. Furthermore, G42 is the first iZIP detector ever to be tested at the UMN facility. In regards to data acquisition, the DAQ software and electronics used to collect the data in this thesis are currently under development. Further improvements to these components are expected which will, in turn, produce more accurate results. Also, CDMSBATS and the DAQ configuration are not fully compatible with one another yet. Improvements here will improve data analysis features. Due to the factors mentioned above (though not limited to only those) the results obtained from the analysis are not ideal. Another item to consider is that some analysis procedures were not performed. For example, a relative calibration of the 8 phonon channels to one another was not done. While it is expected that this effect would not be large, it would symmetrize the response of the detector and reduce the thickness of the electron recoil band. This could then help improve identification of nuclear recoil events. Further along these lines, CDMS analyses typically involve extensive gamma calibrations that allow detailed position correction of events (which further reduces the thickness of the electron recoil band). Such extensive gamma calibrations were not performed in this run, and hence there was no attempt to perform the position correction.

The errors accounted for in the data analysis were random statistical errors. For a proper error analysis systematic errors due to equipment and data acquisition/processing would have to be taken into account. For example, improvements with the DAQ and CDMSBATS will provide more accurate timing information for measurements so that the "dead time" between individual event measurements can be ignored. This, in turn, would facilitate an accurate calculation of the ratio of neutron fluxes from the two data sets, which would be a significant improvement over the calculation of scaled neutron counts. Another systematic error that should be accounted for is the placement of the neutron source. The purpose of the shield is to reject ambient neutrons in

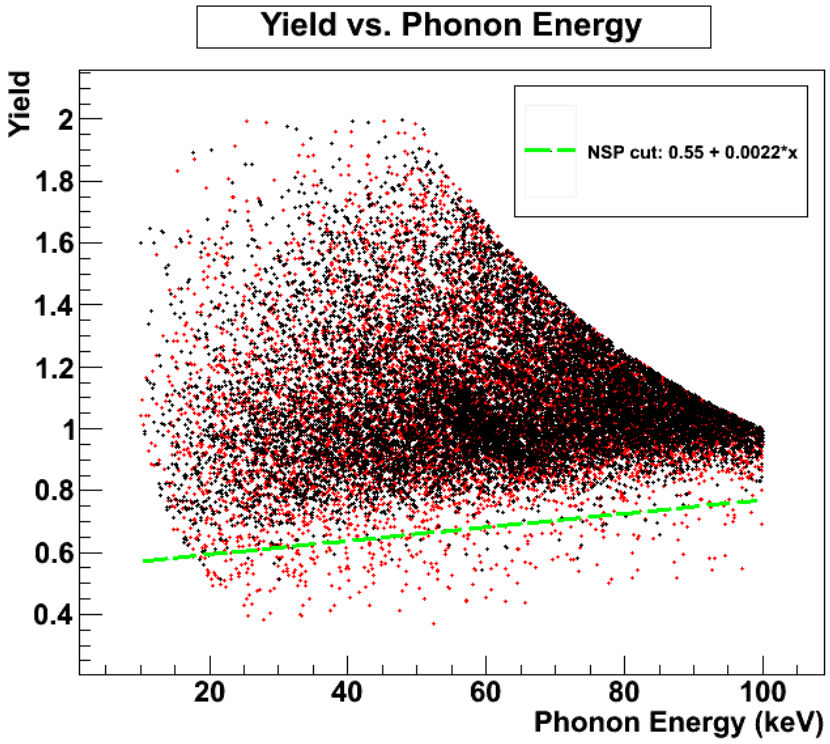


Figure 4.22: An example of selecting a region with neutrons. An NSP value of 0.55 was chosen, cutting out all events above and leaving behind those below the dashed line.

the laboratory. However, the Cf-252 source was used to obtain high statistics in order to clearly identify the shielding effect. It may be that the placement of this source affected the number of neutrons observed by the detector. The shielding above the detector is not as complete as it is around the sides and below, and for the data analyzed in this thesis the source was placed at the side. A test can be done by placing the source above the refrigerator to see if the results of the shield differ significantly. Also, long data sets with and without the shield should be taken to get a better idea of the ambient neutron flux.

In general, more tests with the dilution refrigerator, minus the pressure of testing a detector, will contribute to greater understanding of the equipment and sources of error. With future runs, extensive testing of iZIPS will be performed, and further development of the DAQ software and electronics are already under way. This suggests that an improvement in the analysis is definitely achievable, and also will allow opportunities to better comprehend the systematic errors coming from the experiment.

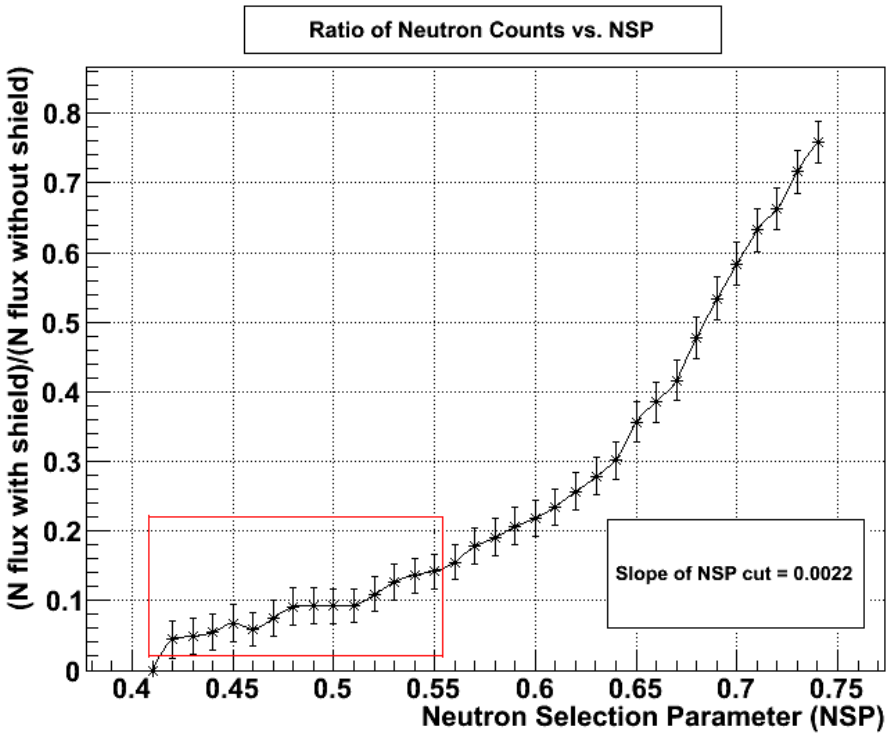


Figure 4.23: Variation in the neutron selection parameter affects the number of nuclear recoil events, as measured in each of the two data sets. The error bars reflect random statistical errors. The ratio of shielded/unshielded nuclear recoil events is roughly constant within the boxed region, which implies that the neutron sample in this region is relatively little contaminated by electron recoil events.

# Chapter 5

# Conclusion

The work discussed in this paper focused on the development and effectiveness of a neutron shield made of high-density polyethylene. The goal for the shield was to reduce the neutron flux interacting with the detector by at least a factor of 10. Based on theoretical calculations it was determined that an 8-inch thick shield of polyethylene would provide sufficient suppression. A shield with this thickness was constructed to surround the detector (except for directly above, where limited space reduced the thickness and coverage of the shielding). After taking appropriate measurements, it was found that the neutron flux suppression due to the neutron shield was indeed consistent with a factor of at least 10. However, data acquisition software and electronics are still under development and UMN's experience with iZIP detectors is not yet extensive. With hopes of improved equipment and software and future runs with different iZIP detectors, more tests with the shield will most certainly provide better results on its capabilities. The systematics of the equipment are also an area of the experiment that will need to be further understood. The next step in the development of the neutron shield is to place more polyethylene within the dilution refrigerator. Recall from Chapter 3 that only 1.5 inches of polyethylene was placed within the inner can. There is a spatial limitation caused by the detector tower structure due to the nature of the read-out wire configuration. If the side-coaxial holders for the read-out wires can be removed and a new wiring design is implemented, then this removes the need for the detector tower. This will allow for more polyethylene to placed within the can directly above the detector, thus providing a more complete coverage of the detector from neutrons. If this new wiring technique proves successful, it is possible that this may be adopted for future use within CDMS.

# Bibliography


[1] Direct Detection of Dark Matter, Sensitivity plotter, July 2011. http://dmtools.brown.edu/.

[2] WMAP- Seven Year Cosmological Parameters, April 2011. http://lambda.gsfc.nasa.gov/.

[3] L. Abbott. The Mystery of the Cosmological Constant. *Sci. Am.*, 258:106–113, May 1988.

[4] M. Aleska and C.W. Fabjan. Fundamental physics with noble liquid detectors. In *Dielectric Liquids, 2005. ICDL 2005. 2005 IEEE International Conference on*, pages 1–12, June-1 July 2005.

[5] V. Barger, Y. Gao, and D. Marfatia. Dark matter at DeepCore and IceCube. *Phys. Rev.*, D83, 2011. 055012.

[6] J. Carr, G. Lamanna, and J. Lavalle. Indirect detection of dark matter. *Rep. Prog. Phys.*, 69, 2006. 2475-2512.

[7] E. Aprile et al. Dark matter results from 100 live days of XENON100 data, April 2011. arXiv:1104.2549v2 [astro-ph.CO].

[8] D.S. Akerib et al. Exclusion limits on the WIMP-nucleon cross-section from the first run of the Cryogenic Dark Matter Search in the Soudan Underground Lab. *Phys. Rev.*, D72, 2005. 052009, astro-ph/0507190.

[9] J. Cherwinka et al. A search for the dark matter annual modulation in South Pole ice, Jun 2011. arXiv:1106.1156v1 [astro-ph.HE].

[10] O. Adriani et al. An anomalous positron abundance in cosmic rays with energies 1.5-100 GeV. *Nature*, 458:607–610, Apr 2009.

[11] R. Bernabei et al. First results from DAMA/LIBRA and the combined results with DAMA/NaI, April 2008. arXiv:0804.2741v1 [astro-ph].

[12] R. Bernabei et al. The DAMA/LIBRA apparatus, April 2008. arXiv:0804.2738v1 [astro-ph].

[13] Z. Ahmed et al. Dark matter search results from the CDMS II experiment. *Science*, 327, March 2010.

[14] K.Nakamura et al. (Particle Data Group). *J. Phys*, G 37, 2010. 075021, Detectors for non-accelerator physics, sec. 29 (S. Golwala).

[15] K. Freeman. Dark matter in galaxies. *Encyclopedia of Astronomy and Astrophysics*, 2001.

[16] W. L. Freeman. Determination of cosmological parameters. *Physica Scripta*, T85:37–46, 2000.

[17] R. J. Gaitskell. Direct detection of dark matter. *Annu. Rev. Nucl. Part. Sci.*, 54:315–59, 2004.

[18] S. R. Golwala. *Exclusion limits on WIMP-nucleon elastic-scattering cross section from the Cryogenic Dark Matter Search*. PhD thesis, 2000.

[19] S. Hertel. IZIP Revisions for Soudan Implementation, June 2010. Internal Note.

[20] W.N. Hess, H. W. Patterson, and R. Wallace. Cosmic-ray neutron energy spectrum. *Physical Review*, 116(2), Oct. 1959.

[21] G. Jungman, M. Kamionkowski, and K. Griest. Supersymmetric dark matter. *Physics Reports*, 267, 1996.

[22] E.W. Kolb and M.S. Turner. *The Early Universe*. Addison-Wesley Publishing Company, 1994.

[23] M. Ackerman et al. Constraints on Dark Matter Annihilation in Clusters of Galaxies with the Fermi Large Area Telescope, April 2010. arXiv:1002.2239v4 [astro-ph.CO].

[24] C.H. Mesquita, T.M. Filho, and M.M.Hamada. Development of neutron detector using the PIN photodiode with polyethylene (n,p) converter. *IEEE Trans. on Nucl. Sci.*, 50(4):1170–1175, Aug 2003.

[25] J.P. Ostriker, P.J.E Peebles, and A. Yahil. The size and mass of galaxies and the mass of the universe. *Astrophysical Journal*, 193(2), Oct. 1974. L1-L4.

[26] A. Reisetter. Monte-Carlo simulation of Soudan Mine neutron energy spectrum. Private communication.

[27] P. Rinard. Neutron interactions with matter. In *In Passive Nondestructive Assay of Nuclear Material, Los Alamos Technical Report*, pages 357–377, 1991.

[28] C. Rott. Indirect searches for dark matter with IceCube. *J.Phys.*, 2008. Conf. Ser. 120 022009.

[29] B. Serfass. Ambient neutron flux measured at UCB . Private communication.

[30] Shieldwerx. *SWX-213 (Pure Poly) Properties*, July 2008.

[31] P. Ullio, M. Kamionkowski, and P. Vogel. Spin-dependent WIMPs in DAMA. *JHEP*, 44, July 2001.

[32] School of Physics & Astronomy Machine Shop University of Minnesota. Platform design for neutron shield.

[33] C. Wiebusch. Physics capabilities of the IceCube DeepCore detector, Jul 2009. arXiv:0907.2263v1 [astro-ph.IM].

[34] L. L. R. Williams, 2010. Lectures on cosmology.

[35] Z. Ahmed et al. Results from the final exposure of the CDMS II experiment, Dec 2009. arXiv:0912.3592v1 [astro-ph.CO].

[36] F. Zwicky. The redshift of extragalactic nebulae. *Helv. Phys.*, Acta 6:110–127, 1933.